

UNIVERSIDADE FEDERAL DO ABC

PROGRAMA DE PÓS-GRADUAÇÃO EM NANOCIÊNCIAS E MATERIAIS

AVANÇADOS

Julia Delatorre Bronzato Zazyki

SÍNTESE E INTERAÇÃO DE NANOESTRUTURAS DE

ÓXIDOS METÁLICOS COM BIOMOLÉCULAS

Santo André, SP

2023

JULIA DELATORRE BRONZATO ZAZYKI

**SÍNTESE E INTERAÇÃO DE NANOESTRUTURAS DE
ÓXIDOS METÁLICOS COM BIOMOLÉCULAS**

Thesis presented to the Nanosciences and
Advanced Materials Graduate Program of
the Federal University of ABC as a partial
requirement to obtain the title of Doctor
of Nanosciences and Advanced Materials.

Supervisor: Prof^a Dr^a Iseli Lourenço
Nantes

Santo André

2023

Sistema de Bibliotecas da Universidade Federal do ABC
Elaborada pelo Sistema de Geração de Ficha Catalográfica da UFABC
com os dados fornecidos pelo(a) autor(a).

Delatorre Bronzato Zazyki, Julia
Síntese e Interação de Nanoestruturas de Óxidos Metálicos com
Biomoléculas / Julia Delatorre Bronzato Zazyki. — 2023.

89 fls.

Orientadora: Iseli Lourenço Nantes

Tese (Doutorado) — Universidade Federal do ABC, Programa de
Pós-Graduação em Nanociências e Materiais Avançados, Santo André, 2023.

1. nanoparticles. 2. quantum dots. 3. cobalt oxide. 4. biomolecules. 5. green
synthesis. I. Lourenço Nantes, Iseli. II. Programa de Pós-Graduação em
Nanociências e Materiais Avançados, 2023. III. Título.

Este exemplar foi revisado e alterado em relação à versão original, de acordo com as observações levantadas pela banca examinadora no dia da defesa, sob responsabilidade única do(a) autor(a) e com a anuência do(a) (co)orientador(a).



MINISTÉRIO DA EDUCAÇÃO

Fundação Universidade Federal do ABC

Avenida dos Estados, 5001 – Bairro Santa Terezinha – Santo André – SP
CEP 09210-580 · Fone: (11) 4996-0017

Ata de Defesa de Tese de Doutorado

No dia 28 de Fevereiro de 2023 às 14h00, Online, realizou-se a Defesa de Tese de Doutorado, que constou da apresentação do trabalho intitulado “**Síntese e Interação de Nanoestruturas de Óxidos Metálicos com Biomoléculas**” de autoria da candidata, **JULIA DELATORRE BRONZATO ZAZYKI**, RA nº 23201910563, discente do Programa de Pós-Graduação em NANOCIÊNCIAS E MATERIAIS AVANÇADOS da UFABC. Concluídos os trabalhos de apresentação e arguição, a candidata foi considerada APROVADA pela Banca Examinadora.

E, para constar, foi lavrada a presente ata, que vai assinada pelos membros da Banca.

Prof.(a) ALEXANDRE JOSE DE CASTRO LANFREDI

UNIVERSIDADE FEDERAL DO ABC - Membro Titular

Documento assinado digitalmente



ARYANE TOFANELLO DE SOUZA
Data: 02/03/2023 08:43:49-0300
Verifique em <https://verificador.iti.br>

Prof.(a) ARYANE TOFANELLO DE SOUZA

UNIVERSIDADE FEDERAL DO ABC - Membro Titular

Documento assinado digitalmente



MARCIA TSUYAMA ESCOTE
Data: 03/03/2023 17:53:41-0300
Verifique em <https://verificador.iti.br>

Prof.(a) MARCIA TSUYAMA ESCOTE

UNIVERSIDADE FEDERAL DO ABC - Membro Titular

Documento assinado digitalmente



WANIUS JOSE GARCIA DA SILVA
Data: 02/03/2023 08:05:12-0300
Verifique em <https://verificador.iti.br>

Prof.(a) WANIUS JOSE GARCIA DA SILVA

UNIVERSIDADE FEDERAL DO ABC - Membro Titular

Documento assinado digitalmente



MARCELO YUDI ICIMOTO
Data: 02/03/2023 11:16:36-0300
Verifique em <https://verificador.iti.br>

Prof.(a) MARCELO YUDI ICIMOTO

UNIVERSIDADE FEDERAL DE SÃO PAULO - Membro Suplente

Prof.(a) PATRÍCIA TARGON CAMPANA

- Membro Suplente
Documento assinado digitalmente



ISELI LOURENCO NANTES
Data: 03/03/2023 19:14:36-0300
Verifique em <https://verificador.iti.br>

Prof.(a) ISELI LOURENCO NANTES

UNIVERSIDADE FEDERAL DO ABC - Presidente

* Por ausência do membro titular, foi substituído pelo membro suplente descrito acima: nome completo, instituição e assinatura



Universidade Federal do ABC



MINISTÉRIO DA EDUCAÇÃO

Fundação Universidade Federal do ABC

Avenida dos Estados, 5001 – Bairro Santa Terezinha – Santo André – SP
CEP 09210-580 · Fone: (11) 4996-0017

Ressalvas e sugestões da Banca examinadora:

Conforme Resolução da CPG nº 05, de 26 de abril de 2016, os membros que participaram de modo remoto, pelos quais o Presidente da Banca assinou no anverso desta Ata, foram:

Por sugestão da Banca Examinadora, o novo título passa a ser (em letra de forma e legível):

Assinatura do Presidente da Banca (apenas em caso de alteração)

* Por ausência do membro titular, foi substituído pelo membro suplente descrito acima: nome completo, instituição e assinatura



Universidade Federal do ABC



MINISTÉRIO DA EDUCAÇÃO

Fundação Universidade Federal do ABC

Avenida dos Estados, 5001 – Bairro Santa Terezinha – Santo André – SP
CEP 09210-580 - Fone: (11) 4996-0017

FOLHA DE ASSINATURAS

Assinaturas dos membros da Banca Examinadora que avaliou e aprovou a Defesa de Tese de Doutorado da candidata, JULIA DELATORRE BRONZATO ZAZYKI realizada em 28 de Fevereiro de 2023:

Prof.(a) ALEXANDRE JOSE DE CASTRO LANFREDI

UNIVERSIDADE FEDERAL DO ABC

Documento assinado digitalmente



ARYANE TOFANELLO DE SOUZA
Data: 02/03/2023 08:40:45-0300
Verifique em <https://verificador.iti.br>

Prof.(a) ARYANE TOFANELLO DE SOUZA

UNIVERSIDADE FEDERAL DO ABC

Documento assinado digitalmente



MARCIA TSUYAMA ESCOTE
Data: 03/03/2023 17:55:34-0300
Verifique em <https://verificador.iti.br>

Prof.(a) MARCIA TSUYAMA ESCOTE

UNIVERSIDADE FEDERAL DO ABC

Documento assinado digitalmente



WANIUS JOSE GARCIA DA SILVA
Data: 02/03/2023 08:01:56-0300
Verifique em <https://verificador.iti.br>

Prof.(a) WANIUS JOSE GARCIA DA SILVA

UNIVERSIDADE FEDERAL DO ABC

Documento assinado digitalmente



MARCELO YUDI ICIMOTO
Data: 02/03/2023 11:18:05-0300
Verifique em <https://verificador.iti.br>

Prof.(a) MARCELO YUDI ICIMOTO

UNIVERSIDADE FEDERAL DE SÃO PAULO

Prof.(a) PATRÍCIA TARGON CAMPANA

Documento assinado digitalmente



ISELI LOURENCO NANTES
Data: 01/03/2023 17:08:47-0300
Verifique em <https://verificador.iti.br>

Prof.(a) ISELI LOURENCO NANTES

UNIVERSIDADE FEDERAL DO ABC

* Por ausência do membro titular, foi substituído pelo membro suplente descrito acima: nome completo, instituição e assinatura



Universidade Federal do ABC

This study was financed in part by the Coordenação de Aperfeiçoamento de Pessoal de Nível Superior - Brasil (CAPES) - Finance Code 001.

Agradecimentos

Desejo agradecer a todos que, de alguma forma, participaram e permitiram que essa tese se concretizasse. Em primeiro lugar, a Deus, no qual possuo uma fé inabalável, que sempre esteve presente em minha vida, e que me deu força nos momentos mais difíceis dessa etapa. A minha família por sempre me apoiar. A meu pai Rinaldo Bronzato, minha mãe Cintia Maura Delatorre Bronzato e minha irmã Juliana Delatorre Bronzato Ximenes, que acreditaram desde o começo em mim, me apoiaram e me incentivaram a seguir meus sonhos. A meu marido, Marco Aurélio Denis Zazyki, pelo permanente incentivo, paciência e amor demonstrados nessa jornada. A minha orientadora, Dr^a Iseli Lourenço Nantes, por ter me recebido em seu laboratório e por ter acreditado em mim e nas minhas capacidades. À Universidade Federal do ABC e à Central Multiusuário UFABC, que disponibilizaram suas instalações para que a pesquisa fosse realizada. Aos demais professores e colegas de laboratório, cada qual com sua capacidade e especialidade, que auxiliaram nos experimentos e contribuíram para os artigos publicados. Ao Laboratório Nacional de Nanotecnologia, do Centro Nacional de Pesquisas em Energia e Materiais, pelas análises e aquisições de imagens das nanopartículas desenvolvidas. À CAPES e CNPq. E por fim, mas não menos importante, à FAPESP pelo financiamento da bolsa de estudos do doutorado, processo FAPESP nº 2019/01425-1.

RESUMO

O óxido de cobalto (Co_3O_4) é um material com uma diversidade de aplicações, e as propriedades desejáveis são aprimoradas na estrutura nano cristalina. Diversas técnicas foram desenvolvidas para a síntese de Co_3O_4 . Algumas rotas fazem uso de biomoléculas como coadjuvantes usando proteínas purificadas, como ferritina e extratos de plantas. No presente estudo, nitrato de cobalto (II) hexahidratado $[\text{Co}(\text{NO}_3)_2 \cdot 6\text{H}_2\text{O}]$ foi utilizado para a síntese de nanopartículas (NPs) de óxido de cobalto com extrato de tomate sob agitação, seguida de acidificação e alcalinização, sempre em alta rotação à temperatura ambiente, e sem controle de atmosfera. Investigação mais aprofundada mostrou ser o alto teor de ferritina, responsável pela eficiência desse vegetal na produção de óxidos metálicos nano particulados. A ferritina está presente em espécies animais e vegetais e é uma fonte verde, barata e fácil de síntese de óxido de cobalto com importantes aplicações tecnológicas. É uma proteína de armazenamento de ferro composta por 24 cadeias polipeptídicas ricas em α -hélice. No presente estudo, o material nano particulado foi sintetizado com semente de tomate tipo “Carmen”, e com a ferritina do baço de cavalo. No processo de síntese não houve acréscimo de agente redutor, estabilizante ou solvente apolar ou orgânico. Após caracterizações mais profundas, as nanopartículas de óxido de cobalto foram chamadas de quantum dots (QDs), devido ao seu tamanho ser menor que 5 nm. Foram realizadas caracterizações por espectrofotometria UV-visível, microscopia eletrônica de transmissão de alta resolução (HRTEM), espectrômetro de fotoelétrons excitados por raios-X (XPS), espectrômetro infravermelho por transformada de Fourier (FTIR) e dispositivo supercondutor de interferência quântica (SQUID). Co_3O_4 QDs apresentaram quiralidade evidenciada por dicroísmo circular magnético. Consistente com os dados anteriores de Mössbauer, a ressonância paramagnética eletrônica (EPR) revelou a presença da ferritina de ferro como o sinal de íon de ferro dominante em sementes de tomate. A ferritina do baço de cavalo foi igualmente eficiente na produção de Co_3O_4 QDs.

Palavras-chave: nanopartículas, quantum dots, óxido de cobalto, biomoléculas, síntese verde.

ABSTRACT

Cobalt oxide (Co_3O_4) is a material with a variety of applications, and the desirable properties are enhanced in the nano crystalline structure. Several techniques have been developed for the synthesis of Co_3O_4 . Some routes use biomolecules as co-adjuvants using purified proteins, such as ferritin, and plant extracts. In the present study, cobalt (II) nitrate hexahydrate $[\text{Co}(\text{NO}_3)_2 \cdot 6\text{H}_2\text{O}]$ was used for the synthesis of cobalt oxide nanoparticles (NPs) and quantum dots (QDs) with tomato extract under agitation, followed by acidification and submission to high speed at room temperature, without atmosphere control. Further investigation showed that the high content of ferritin is responsible for the efficiency of this plant in the production of nanoparticulated metal oxides. Ferritin is present in animal and plant species and is a green, inexpensive and easy source of cobalt oxide synthesis with important technological applications. It is an iron storage protein composed of 24 polypeptide chains rich in α -helix. In the present study, the nanoparticulated material was synthesized with different variations; with “Carmen” tomato seed and pulp and with horse spleen ferritin. In the process of synthesis of Co_3O_4 NPs/QDs, there was no addition of a reducing agent, stabilizer, or nonpolar or organic solvent. QDs and NPs were characterized by UV-visible spectrophotometry, high-resolution transmission electron microscopy (HRTEM), X-ray excited photoelectron spectrometer (XPS), Fourier transform infrared spectrometer (FTIR), and superconducting quantum interference device (SQUID). Co_3O_4 QDs showed chirality evidenced by magnetic circular dichroism. Consistent with previous Mössbauer data, electronic paramagnetic resonance (EPR) revealed the presence of iron ferritin as the dominant iron ion signal in tomato seeds. Horse spleen ferritin was equally efficient in the production of Co_3O_4 QDs.

Keywords: nanoparticles, quantum dots, cobalt oxide, biomolecules, green synthesis.

List of figures

Figure 1. Applications of metal oxides.....	13
Figure 2. Methods to synthesize nanoparticles.....	15
Figure 3. Energy diagram	16
Figure 4. Ferritin molecule.	17
Figure 5. Scheme of a ferritin molecule.	18
Figure 6. Synthesis of Co_3O_4 QDs using tomato seed extract.....	29
Figure 7. UV-visible spectra of Co_3O_4 QDs and the corresponding Tauc plots.	30
Figure 8. High-resolution transmission electron microscopy (HRTEM) of Co_3O_4 QDs	32
Figure 9. ZFC and FC curves of Co_3O_4 QDs	33
Figure 10. XPS spectrum of Co_3O_4 QDs.....	34
Figure 11. Characterization of chiral Co_3O_4 QDs – CD and MCD.....	37
Figure 12. Antiviral application of Co_3O_4 QDs.....	39
Figure 13. FTIR analysis of the effect of Co_3O_4 QDs on phosphatidylcholine.....	41
Figure 14. CIPRO chemical structure with its ionizable groups with respective pK_a values. .	47
Figure 15. E.coli in Gram stain showing Gram-negative bacilli.	50
Figure 16. High-resolution transmission electron microscopy (HRTEM) of the QDs.	52
Figure 17. Changes in Cipro spectrum during exposure to a solar simulator and UV light in the absence and presence of Co_3O_4 QDs	54
Figure 18. FTIR spectra of CIPRO exposed to UV irradiation under different conditions.	56
Figure 19. The Etest method	58
Figure 20. Effect of irradiation and Co_3O_4 QDs on CIPRO degradation	60
Figure 21. The HRTEM of the Au and Fe_3O_4 nanoparticles produced with tomato extract....	77
Figure 22. UV-Visible spectra and the corresponding Tauc plots of the nanoparticles synthesized with D CHA (left image) and L CHA (right image).....	80
Figure 23. FEG images and NTA – D CHA.	81
Figure 24. FEG images and NTA – L CHA.	82
Figure 25. X-ray diffraction spectra of the NPs synthesized with L CHA and D CHA.....	83
Figure 26. Circular dichroism (CD) spectra L CHA and D CHA	84

List of abbreviations

CD: Circular Dichroism

CHA: Peptide formed by the amino acids Cysteine, Histidine, and Alanine

EPR: Electron Paramagnetic Resonance

FESEM-EDX: field emission scanning electron microscopy with energy dispersive X-ray spectroscopy,

FTIR: Fourier Transform Infrared Spectrometer

HRTEM: High-resolution Transmission Electron Microscopy

MCD: Magnetic Circular Dichroism

NP: Nanoparticle

NTA: Nanoparticle Tracking Analysis

QD: Quantum Dot

SQUID: Superconducting Quantum Interference Device

XPS: X-ray Excited Photoelectron Spectrometer

XRD: X-ray Diffraction Spectra

SUMMARY

1. INTRODUCTION	13
1.1. Metal oxides	13
1.1.2. Nanoparticles	14
1.2. Biomolecules as templates.....	17
2. OBJECTIVES.....	19
3. CHAPTER 1.....	20
ABSTRACT	21
3.1. Introduction	22
3.2. Material and methods	24
3.2.1. Chemicals	24
3.2.2. Synthesis of noble metal nanoparticles	24
3.2.3. Spectroscopic measurements.....	25
3.2.3.1. UV-visible absorbance measurements.....	25
3.2.3.2. Circular dichroism (CD) and Magnetic Circular (MCD) spectroscopy	25
3.2.3.3. Determination of nanoparticle size, crystal structure, and composition by high-resolution transmission electron microscopy (HRTEM).....	25
3.2.3.4. FTIR spectroscopy.....	25
3.2.4. Magnetic measurements	26
3.2.4.1. Superconducting quantum interference device measurements.....	26
3.2.4.2. Electron paramagnetic resonance (EPR)	26
3.2.5. Application of Co ₃ O ₄ QDs	27
3.2.5.1. Production of virucidal 100% cotton fabric	27
3.2.5.2. Virucidal Assay	27
3.3. Results and discussion.....	28
3.3.1. Virucidal activity	38
3.4. Conclusion	43
4. CHAPTER 2.....	44
ABSTRACT	45
4.1. Introduction	46

4.2. Material and methods	48
4.2.1. Chemicals	48
4.2.2. Synthesis and characterization of Co ₃ O ₄ quantum dots produced with tomato seed extracts.....	48
4.2.3. UV-visible spectroscopy.....	49
4.2.4. FTIR spectroscopy.....	49
4.2.5. Application of Co ₃ O ₄ QDs for CIPRO photodegradation	49
4.2.6. Microbiological tests	50
4.2.7. Etest	50
4.2.8. Agar diffusion test	51
4.3. Results and discussion	51
4.4. Conclusion	60
 5. CONCLUSION	 62
 REFERENCES	 63
 APPENDIX A - Previous research.....	 75
 APPENDIX B - Future perspectives	 79

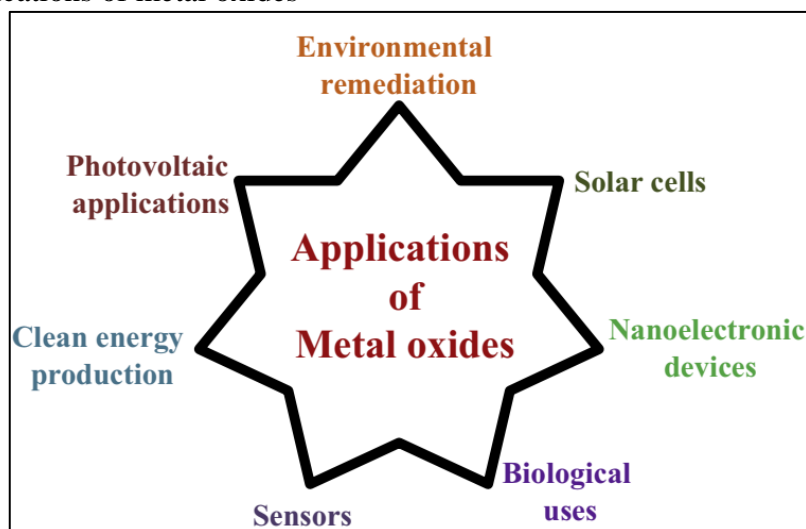
1. INTRODUCTION

1.1. Metal oxides

Metal oxides can generate charge deliverers when stimulated with energy; that's why they are important in electronics and environmental remediation. Most metal oxides have applications in photocatalysis, because of their electronic structure, light absorption, and charge transport properties (KHAN; ADIL; AL-MAYOUF, 2015). The photo catalytic performance depends on the shape, size, composition, and morphology of the metal oxide (DJURIŠIĆ; LEUNG; CHING NG, 2014; HISATOMI; KUBOTA; DOMEN, 2014).

There are many other applications for metal oxide materials (Fig. 1) such as environmental remediation, solar cells, nano electronic devices, biological uses, sensors, clean energy production, and photovoltaic (CHAN et al., 2011; KHAN; ADIL; AL-MAYOUF, 2015).

Figure 1. Applications of metal oxides



Source: (KHAN; ADIL; AL-MAYOUF, 2015).

Some metal oxides such as Co_3O_4 and CoO_x are supercapacitors materials, and are promising due to their pseudo capacitance properties (LIU; PELL; CONWAY, 1999), for example, the thin films of these materials showed capacitor behavior when used as positive electrode (SRINIVASAN; WEIDNER, 2002). This metal oxide can be also found in low,

intermediate, and high spin states, which is attractive to the spintronics and physics of the material (DIALLO et al., 2015).

Metal oxide nanostructures have unique electronic structures, such as metallic, semiconducting (between metals and nonmetals), or insulating properties; they are a lot cheaper than metal nanostructures and are easily synthesized (VAYSSIERES et al., 2001). The synthetic procedure for the preparation of the powder or film is very important to reach the desired properties, size, purity, and shape (VOON et al., 2020; ZHOU; YU; JARONIEC, 2014).

The methods reported in the literature to synthesize are precipitation, hydrothermal, chemical vapor deposition, sol-gel, and microwave-assisted, among others bottom-up and top-down approaches. Nanostructured materials have enhanced properties compared to bulk materials, making it possible to work at atomic and molecular levels, with desired properties and characteristics, according to the chosen synthesis method (MALWAL; PACKIRISAMY, 2018). Metal oxide nanomaterials enhance the properties of catalysts mainly because of their high specific surface area, quantum confinement effects, and charge transport, attracting the interest of researchers (TATON, 2002).

1.1.2. Nanoparticles

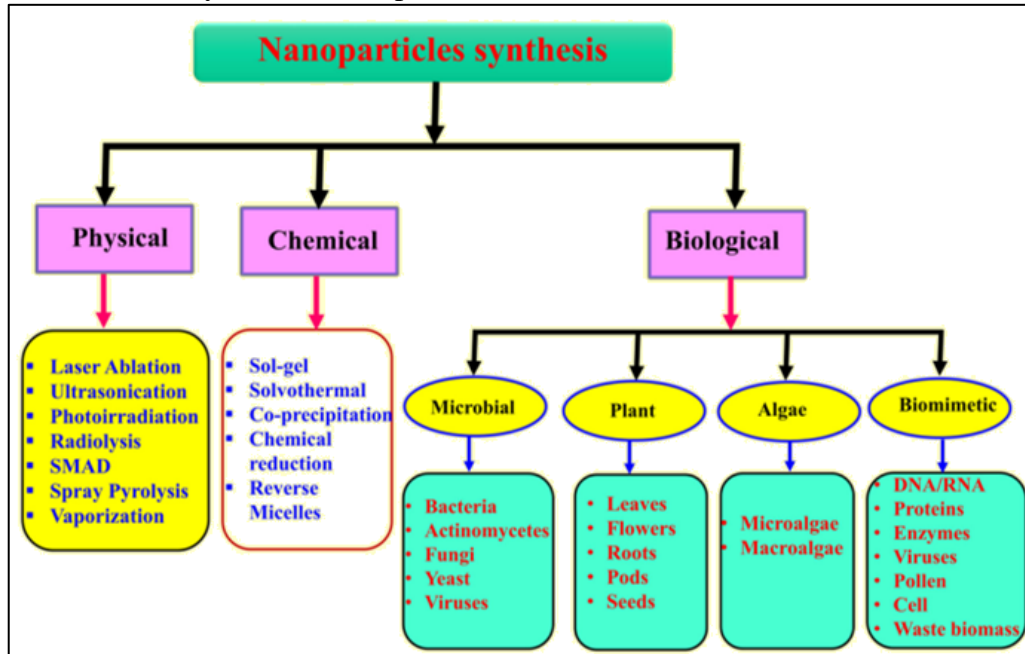
Nanoparticles (NPs) have attracted attention due to their enhanced properties compared to bulk materials, such as catalytic, magnetic, electrical, and optical (NASSAR; AHMED, 2011; XU et al., 2014). They are particles with size range from 1nm to 100nm (KHAN; SAEED; KHAN, 2019). The NPs of transition metal oxides have interesting properties, alike other metals (KUNDU et al., 2013), due to their chemical stability (KUNDU et al., 2013) and great use in industry (TANG; WANG; CHIEN, 2008).

Cobalt oxide is one of them, it has applications in gas sensors, pigments, Li-ion batteries, supercapacitors, solar energy storage, and magnetic materials (DUYNE, 2003; GENG et al., 2008; KUNDU et al., 2013; NAVEEN; SELLADURAI, 2015; NGUYEN; EL-SAFETY, 2011; XU et al., 2014).

Some routes of NPs synthesis are presented in Fig. 2, and can be physical, chemical, or biological (SARATALE et al., 2018). The most common syntheses of crystalline

nanoparticles involve calcination processes with high temperatures, a lot of chemicals, and toxic and expensive precursors (FARHADI; JAVANMARD; NADRI, 2016).

Figure 2. Methods to synthesize nanoparticles.



Source: (SARATALE et al., 2018)

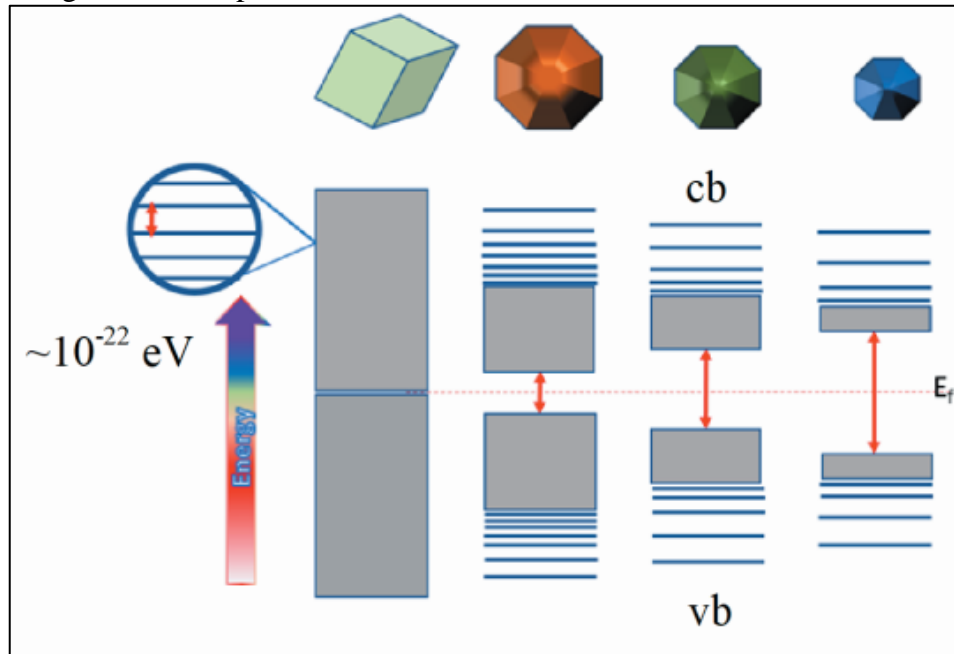
Nowadays, the demand for the production of advanced materials through low-cost, green, and sustainable methods is increasing. Therefore, alternative methods for the synthesis of Co_3O_4 nano crystals assisted by purified biomolecules and plant extracts, in mild conditions, have been developed (KOMBAIAH et al., 2019).

Moreover, nanoparticles can be also characterized as quantum dots (QDs), which have attracted attention recently (BURDA et al., 2005) for their unique properties regarding their size (NOZIK et al., 2010). The bandgap of the nanomaterial will be increased when the size is decreased, once the size is close to its exciton Bohr radius (ALIVISATOS, 1996).

The surface states (electronic quantum states associated with the surface) have effects on the optical properties of the QDs, because of their high surface-to-volume ratio (WANG; HERRON, 1991). Quantum dots are small systems that have a single spin to build light or electric field-manipulated systems. In electronics, for example, can be used in quantum computing (MAEKAWA, 2006). Like bulk materials, quantum dots (QDs) also have a solid-solid phase transition, and this transition influences the optical properties of QDs (TOLBERT et al., 1994).

Quantum dots are considered nanomaterials, so they are located between atoms and bulk materials. The band gap is located between the conduction band (cb) and the valence band (vb). The smaller the number of atoms of the material, the bigger the band gap difference. In other words, microscopic materials have a smaller band gap compared to nanomaterials (fig. 3).

Figure 3. Energy diagram. As the number of atoms decrease, the band gap energy increases. From left to right, microscopic to nanostructured materials.



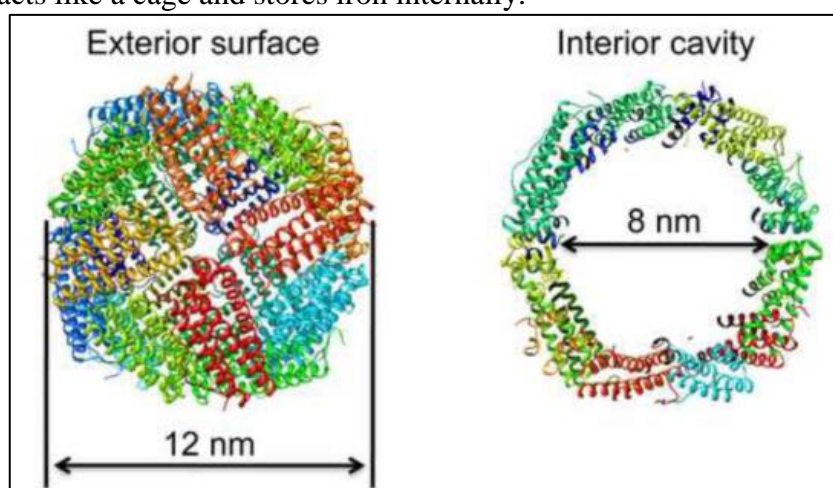
Source: (BRITO et al., 2019)

There are two main properties of the size in QDs. The first one is the increase of the bandgap energy, which means that the diameter is small, this is known as quantum confinement (YOFFE, 2001). The bandgap varies with the composition and size of the semiconductor. The second one is the electronic states of each level, which are atomic-like, well-separated energy states, caused by the low quantity of atoms compared to bulk, in QDs (BERA et al., 2010).

1.2. Biomolecules as templates

Biomolecules and plant extracts can be used to synthesize nanoparticles; ferritin is one of them, it is an iron storage protein composed of 24 polypeptides, can accommodate up to 4500 Fe atoms (HOSEIN et al., 2004), and has an inner diameter of 8nm and an outer of 12nm (Fig. 4) (HUANG et al., 2014; UCHIDA et al., 2014). According to the literature, the core of the ferritin can be removed, in a pH-induced unfolding–refolding process for example, and the metal complexes are introduced into the cage (Fig. 5) (HIKONO et al., 2003).

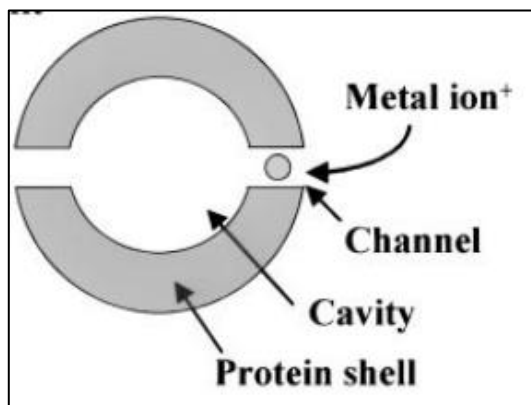
Figure 4. Ferritin molecule. The inner diameter is 8nm and the outer is 12nm. The protein with the core acts like a cage and stores iron internally.



Source: (UCHIDA et al., 2014)

The iron atoms from the ferritin core can be removed by reducing agents and Fe(II) chelation. Other ions such as copper, cobalt, and nickel can bind in the apoferritin (the hollow core of ferritin), making it a biotemplate for green and size-controlled synthesis of nanostructures (WANG et al., 2016a) (KASYUTICH et al., 2010). The protein shell has junctions pores that allow the passage of ions and small molecules (Fig. 5) (KASYUTICH et al., 2010).

Figure 5. Scheme of a ferritin molecule. The protein with the core acts like a cage and stores iron internally.



Source: (HIKONO et al., 2003)

The pores of the shell are hydrophilic, negatively charged with residues, and absorb ions Fe(II); the iron is attracted, enters the channels, reaches the cavity, and is oxidized by molecular oxygen becoming Fe (III) (Fig. 5) (CHIANCONE et al., 2004).

Extracts from plants, such as leaves, seeds, fruits, and roots have been described as efficient sources of reducing and stabilizing agents for Co_3O_4 nanostructures synthesis, including quantum dots (PAGAR et al., 2019b; SARATALE et al., 2018). The responsible for reducing, capping, and stabilizing the metal oxides are polyphenols, alkaloids, amino acids, polyols, and carboxylic acids, among others (BORASE et al., 2014; IRAVANI et al., 2014).

In this thesis, the differential is that we were able to synthesize nanoparticles with crude extract of the ferritin and the tomato, without purification and the removal of the iron ion from the core of the ferritin, in a facile and green method that uses few chemicals. Two applications of the nanoparticles were investigated, such as virucidal agent and photodegradation of an antibiotic. Beyond that, an initial investigation using peptides as biotemplates is on appendix B, showing promising results.

2. OBJECTIVES

In the present work, nanoparticles/quantum dots of cobalt oxide were synthesized using tomato extract as a reducing agent without the use of organic solvent precursors or other additives. Two articles will be presented as a result of the work. The first one is about the synthesis of the QDs, characterization, and application as a virucidal agent. The second article shows the photodegradation of the antibiotic ciprofloxacin by the QDs.

The ability of the tomato extract ferritin to capture inorganic ions and promote its hydroxylation to synthesize as nanoparticles was used. The method was carried out at room temperature and without the addition of chemical solvents, enabling industrial application with energy savings and environmental protection. A synthesis with pure ferritin was also carried out to compare the results, and to confirm their participation in the formation of the material.

In this case, the ferrihydrite mineral core present in ferritin acts as a semiconductor capable of catalyzing oxidation/reduction reactions. Ferritin has a pH-modulated denaturation and renaturation capacity. Conditions under acidic conditions, such as ferritin subunits, can dissociate and not denature, reorganizing when the pH is adequate to values close to physiological. During the first stage of the process, iron oxides present in the protein cavity can be released, while other molecules (for example, metal salts) in a solution can do the opposite way and allow the formation of nanoparticles.

In previous research by our group (appendix A), gold and silver salt were used to synthesize gold and silver nanoparticles respectively. We established continuity with the use of other metal salts, to be investigated both for synthesis using tomato extracts and for synthesis using ferritin. The first type of metallic salt other than gold and silver is to be used as cobalt in the form of nitrate. Using cobalt salts, we obtained Co_3O_4 nanoparticles from tomato seeds and pulp and pure ferritin.

3. CHAPTER 1

VIRUCIDAL, PHOTOCATALYTIC AND CHIROMAGNETIC COBALT OXIDE QUANTUM DOTS

Authors: Julia D. Bronzato, Aryane Tofanello, Martha T. Oliveira, Jefferson Bettini, Adrianne M. M. Brito, Silgia A. Costa, Sirlene M. Costa, Alexandre J. C. Lanfredi, Otaciro R. Nascimento and Iseli L. Nantes-Cardoso.

Periodic: Applied Surface Science, volume 576 (2022), pages 151847.

Publication Date: Received 7 July 2021; Received in revised form 25 October 2021; Accepted 6 November 2021; Available online 9 November 2021.

ABSTRACT - Multifunctional quantum dots (QDs) of Co_3O_4 were fabricated using cobalt II nitrate hexahydrate with tomato (*Solanum Lycopersicum* L.) seed extract and were efficiently applied as a virucidal additive in cotton fabric. The low-dimensional semiconductor, exhibiting a quantum confinement regime along with charge carrier confinement, resulted in superior antiviral characteristics. The QDs were characterized by UV-visible spectrophotometry, high-resolution transmission electron microscopy, X-ray excited photoelectron spectrometry, Fourier transform infrared spectroscopy, and magnetic properties using a superconductor quantum interference device. Co_3O_4 QDs exhibit chirality, as evidenced by the magnetic circular dichroism spectrum in the spectral region in which the material absorbs. The high ferritin content in tomato seeds, as evidenced by electron paramagnetic resonance, suggested that this protein acts as a nanocage for the growth of Co_3O_4 . Commercially purified horse spleen ferritin was equally efficient in producing Co_3O_4 QDs. Based on these results, it can be concluded that the multifunctional platform of Co_3O_4 QDs satisfactorily meets the requirements to be an efficient photocatalyst and exhibits the potential to be employed as a semiconductor textile-based to combat/prevent coronavirus disease as sustainable personal protective clothing.

Keywords: Co_3O_4 , quantum dots, chiromagnetic material, ferritin, photocatalysis, virucidal materials.

3.1. Introduction

Cobalt oxide (Co_3O_4), especially featured as nanostructured materials, deserves to be highlighted among the transition-metal oxides because of its applications in sensors, solar energy storage, electrochemical capacitors, supercapacitor Li-ion batteries, and magnetic materials (DUYNE, 2003; GENG et al., 2008; KUNDU et al., 2013; NAVEEN; SELLADURAI, 2015; NGUYEN; EL-SAFETY, 2011; TANG; WANG; CHIEN, 2008; TIAN et al., 2021; WANG et al., 2020b; XU et al., 2014). The surface redox reactivity of Co_3O_4 with a spinel structure makes this material a significant catalyst for a variety of reactions such as sodium borohydride hydrolysis (NETSKINA et al., 2016), CO oxidation (BROQVIST, 2002; HU et al., 2010), antibiotic degradation (BROQVIST, 2002; GUO et al., 2013b), Fischer–Tropsch synthesis (WEN et al., 2014), cyclohexane dehydrogenation (NAUERT et al., 2016; TYO et al., 2012), ethylene oxidation (MA et al., 2010), water splitting (LI et al., 2015), tandem amine homocoupling, and amine-alcohol cross-coupling reactions (KAPUGE et al., 2020). Several methods for the synthesis of Co_3O_4 nanoparticles involve an additional calcination process at high temperatures using toxic and expensive precursors (FARHADI; JAVANMARD; NADRI, 2016). Currently, the demand for advanced materials using low-cost, green, and sustainable methods is increasing. Therefore, several methods for the synthesis of Co_3O_4 nanocrystals assisted by purified biomolecules and plant extracts under mild conditions have been developed (KOMBAIAH et al., 2019), several of which have been described as efficient sources of reducing and stabilizing agents for Co_3O_4 nanostructure synthesis, including quantum dots (QDs) (DEWI; YULIZAR; BAGUS APRIANDANU, 2019; DIALLO et al., 2015; DUBEY et al., 2018; HAN; YANG; LIU, 2015; KOMBAIAH et al., 2018; PAGAR et al., 2019a; SIVACHIDAMBARAM et al., 2017). In addition to their low cost, low toxicity, and biocompatibility, the use of biomolecules allows tuning of the shape, size, and, consequently, the properties of nanostructures. Interestingly, Yeom et al. described the synthesis of Co_3O_4 nanoparticles assisted by D and L cysteine, which promoted D and L chiral distortions in the crystal lattices that gave rise to chiromagnetic nanoparticles (YEOM et al., 2018). The chiroptical activity of the Co_3O_4 nanoparticles with chiral distortions in the visible range was 10 times higher than that of nonparamagnetic nanoparticles of similar size. In another class of molecules, that stand out as a biomolecular template, iron storage proteins, such as ferritin, which provide nanocages for the synthesis of diverse metal oxides (GÁLVEZ et al., 2006, 2008a; TOFANELLO et al., 2021a; UCHIDA et al., 2010a; WANG et al., 2016b), including Co_3O_4 (GÁLVEZ et al., 2008b; JIANG et al.,

2019; TOFANELLO et al., 2021a; UCHIDA et al., 2010b; WANG et al., 2016c). Internalized iron can be removed from the ferritin cavity by chemical reduction or chelation, forming a hollow cage in which different nanocrystals can grow in a controlled manner. Therefore, ferritin nanocages are efficient for the biomineralization of diverse semiconductors that exhibit a photocatalytic response, including the synthesis of Co_3O_4 . Co_3O_4 is a versatile photoresponsive and magnetic material with diverse applications involving photocatalysis (ANH TRAN et al., 2021), water splitting (GHOSH et al., 2020), magnetic resonance imaging (DIALLO et al., 2017), and photodegradation of pollutants (WU et al., 2020). Photodegradation promoted by semiconductors is related to the generation of pro-oxidant species, which is undesirable for energy applications (ZHANG et al., 2018) but useful for material applications in disinfection. As observed for other semiconductors (MENEZES et al., 2019; WU et al., 2020; ZHANG et al., 2018), reactions catalyzed by Co_3O_4 involve the photochemical production of pro-oxidant species such as holes (h^+), hydroxyl radicals (OH^\bullet), and singlet oxygen ($^1\Delta_g\text{O}_2$) (KAPUGE et al., 2020). Therefore, the pro-oxidant properties of Co_3O_4 can be used for microbicidal purposes and catalysis. Regarding the application of semiconductors for microbicide purposes, the emergence of epidemics and pandemics has challenged the world, and the culmination thus far has been the COVID-19 pandemic. Despite the development of vaccines and the search for therapies, the difficulties for rapid immunization in all countries, the emergence of new viral strains, and the real risk of the advent of new diseases caused by viruses, bacteria, and fungi, make the measures of disinfection a preventive strategy that we cannot rule out (TOLEDO et al., 2020). The generation of pro-oxidant species to destroy invading pathogens is used by cells of the immune system. Activated macrophages generate pro-oxidant species via myeloperoxidase, which catalyzes the production of hypochlorous acid from hydrogen peroxide and chloride (DIAS; NANTES; RODRIGUES, 2004; TOLEDO et al., 2020). Electronically excited species are also used by biological systems to combat pathogens. Singlet molecular oxygen production has been detected in all peroxidases, including myeloperoxidase (INGENBOSCH et al., 2021). Biological fighting against pathogens can inspire disinfection strategies. Nanostructured transition metal oxides can produce pro-oxidant species (WU et al., 2020; ZHANG et al., 2018). Here, we describe the scalable synthesis of Co_3O_4 QDs assisted by the native holoferritin content of tomato seeds that showed applicability in the inactivation of enveloped viruses.

3.2. Material and methods

3.2.1. Chemicals

Cobalt(II) nitrate hexahydrate ($\text{Co}(\text{NO}_3)_2 \cdot 6\text{H}_2\text{O}$) and crab-extracted chitosan (85% deacetylation minimum) were purchased from Sigma-Aldrich Corp. (St. Louis, MO, USA). L- α -Phosphatidylcholine Egg PC 99% lipid was purchased from Avanti Polar Lipids (Alabaster, AL, USA). A 100% cotton woven fabric (192.4 g m^{-2}) was used to impregnate chitosan and Co_3O_4 QDs. Fresh tomatoes belonging to the locally named Carmen varieties (ATARASSI et al., 2010) were acquired from local supermarkets (Santo André, SP, Brazil).

3.2.2. Synthesis of metal nanoparticles

Co_3O_4 nanoparticles were synthesized using tomato pulp and seed extracts and cobalt (II) nitrate hexahydrate ($\text{Co}(\text{NO}_3)_2 \cdot 6\text{H}_2\text{O}$). The tomato extract was prepared with 50 g of mature tomato pulp (tomatoes peeled off without seeds) and 30 g of seeds, followed by homogenization in 50 mL of deionized water. The tomato extract solution was not filtered. After homogenization, 50 mL of soluble tomato (1 g/mL) and $\text{Co}(\text{NO}_3)_2 \cdot 6\text{H}_2\text{O}$ 10mM solution were mixed at room temperature under stirring at 10,000 rpm with a high-performance Ultra-Turrax homogenizer. The mixture of the precursors was acidified by the addition of HCl 1M (pH 2) and stirred continuously. Then, the system was alkalized with NaOH 10M (pH 12), and the solution was colored purple, blue, and then olive green. The synthesis process occurred in three steps: i) a mixture of cobalt salt tomato extract followed by high stirring, ii) acidification and high stirring, and iii) alkalization followed by high stirring, which culminates in an olive-green colored solution. The sample was subjected to UV-visible spectroscopy analysis for 16 days when its spectral features indicated the formation of Co_3O_4 nanoparticles. The formation of Co_3O_4 nanoparticles was also suggested by the magnetic behavior of the material that could be attracted by a neodymium magnet. After the formation of the magnetic material, all the nanoparticulated material was triple-washed using centrifugation (14,000 rpm) and the pellet was resuspended in deionized water for characterization using different techniques.

3.2.3. Spectroscopic measurements

3.2.3.1. UV-visible absorbance measurements

This technique was used for the colorimetric analysis of the Co_3O_4 formation. UV-visible measurements were performed using a Varian Cary 50 UV-Visible, which performed a spectral scan in the range of 190–1100 nm with intervals (resolution) of 1 nm. The wavelength scan used different spectral ranges according to the sample to be analyzed.

3.2.3.2. Circular dichroism (CD) and Magnetic Circular (MCD) spectroscopy

These techniques were used to analyze the presence of the chiral distortion of the Co_3O_4 nanocrystals. Circular dichroism (CD) measurements were carried out on a Jasco J-850 spectropolarimeter (Easton, MD, USA) using quartz cuvettes with a 0.1 cm and 0.5 cm optical path bandwidth, at intervals, i.e., with a resolution of 1.0 nm slit, a scanning speed of 200 nm/min, a response of 0.25 s, and 10 accumulations.

3.2.3.3. Determination of nanoparticle size, crystal structure, and composition by high-resolution transmission electron microscopy (HRTEM)

Transmission electron microscopy (TEM, JEOL JEM 2100F) operating at 200 kV was used to investigate the size and morphology of the Co_3O_4 QDs. A 400-mesh carbon-coated copper grid was glow-discharged into a vacuum evaporator (Denton, Moorestown, New Jersey) for a few seconds to ensure hydrophilicity and attractiveness to the nanoparticles. A drop of the Co_3O_4 QD stock suspension was deposited onto the grid and dried before analysis. An energy dispersive spectroscopy (EDS) technique using an Oxford SDD, narrow window X-ray (EDS) detector capable of detecting elements and providing the EDX profile.

3.2.3.4. FTIR spectroscopy

An in situ attenuated total reflectance-Fourier transform infrared (ATR-FTIR) technique has been used to study the capping of QDs and the oxidation of phosphatidylcholine liposomes as a model of the lipid fraction of the viral envelope. L- α -

Phosphatidylcholine Egg PC 99% lipid (30 mM) was added to the samples for 30 min under agitation under visible light and UV light. The cotton fabric with lipids was washed with chloroform, and the solution was collected and placed in an *Eppendorf* vial under agitation for 2 min. The two phases were visually separated in seconds, and the lower phase, containing chloroform, was collected for analysis. To perform the spectral reading of each sample, 10 μL of the solution to be analyzed was deposited on the diamond crystal and waited one minute for the sample to dry. The infrared spectra were recorded on a Varian 640-IR spectrometer fitted with a DLaTGS detector and a PIKE MIRacle™ single reflection horizontal ATR accessory with a ~ 1.8 mm sampling area of the diamond crystal and 45° for the angle of light incidence. All spectra were calculated from 64 scans at a resolution of 4 cm^{-1} , and the air was used as the reference spectrum. The absorption spectra were recorded and converted using a specific spectrometer program (Varian Resolutions Pro software program). The peaks were analyzed and compared after vector normalization of each spectrum using Origin Pro 8.5 (OriginLab Corp., USA).

3.2.4. Magnetic measurements

3.2.4.1. Superconducting quantum interference device measurements

An MPMS®3-SQUID magnetometer (Magnetic Properties Magnetic System - Superconductor Quantum Interference Device) was used for magnetic measurements ($M \times T$) in the temperature range of 2–298 K.

3.2.4.2. Electron paramagnetic resonance (EPR)

EPR spectra were obtained on a Varian E109 EPR X-band (Varian, Palo Alto, CA, USA) using a standard rectangular cavity with field modulation at 100 kHz. Parameters: microwave power of 20 mW, modulation amplitude of 0.4 mT peak-to-peak, gain adjustable for each sample, field scan of 700 mT, time constant of 0.064 s, and scan time of 3 min. For measurements at 77 K, liquid N_2 was used in the Dewar immersion method, and a quartz tube of 3 mm internal diameter was used to insert the sample. An EPR standard was used to calibrate the magnetic field (MgO crystal: Cr^{III} $g = 1.9797$), and the resonance frequency of 9.5146 GHz was measured using a microwave frequency counter.

3.2.5. Application of Co₃O₄ QDs

3.2.5.1. Production of virucidal 100% cotton fabric

The Co₃O₄ QDs were impregnated in cotton fabric according to the following procedure: The cotton fabric was previously treated with 0.5% (m/v) chitosan solution prepared in 5% (m/v) citric acid using a Foulard (Pick-Up 86%). The samples impregnated with chitosan were dried in a vaporizer at 90 °C and treated again in the same way as a solution of Co₃O₄ prepared by diluting 8 ml of the solution (6.5 mg/mL of solid) in 40 ml of distilled water and dried at 40 °C.

3.2.5.2. Virucidal Assay

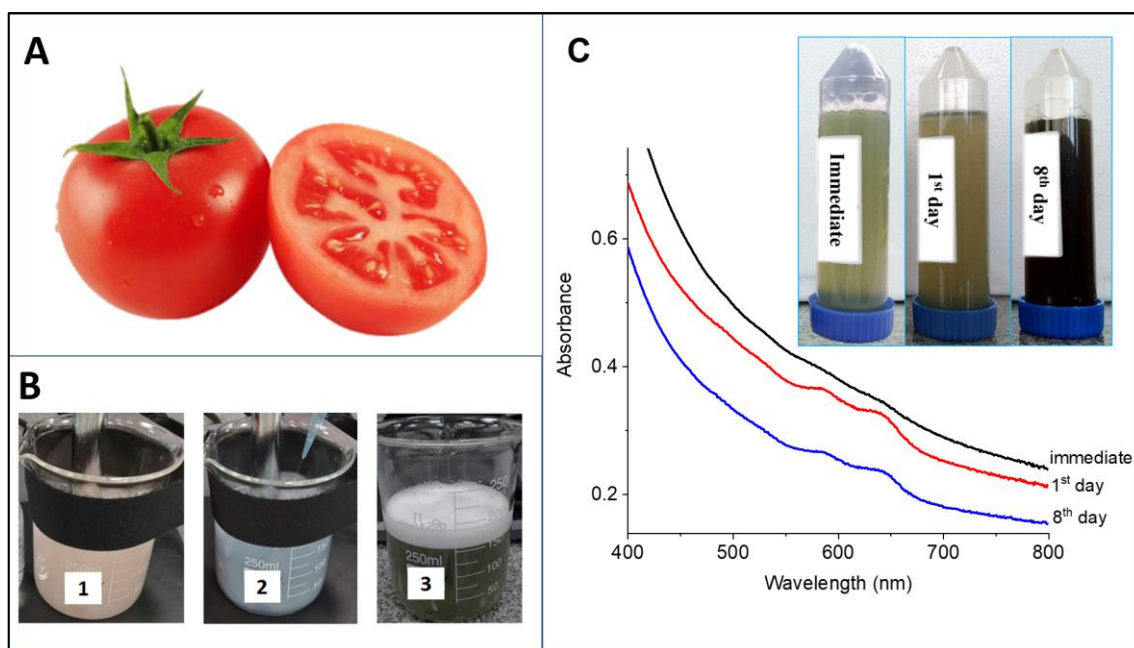
Assays were performed using human coronavirus 229E (HCoV-229E), a single-stranded RNA virus, and MRC-5 cells, a lineage of human pulmonary fibroblasts. The day before the experiments, $2 \cdot 10^4$ cells were seeded per well in 96-well trays. For the virucidal assay, 1 cm² of cotton fabrics (either impregnated with Co₃O₄ QDs or not) were incubated for 5 min with 1000 infectious doses (ID₅₀) of HCoV-229E. Next, 150 µL of the cell culture medium was used to rinse the fabric. All media (~200 µL) were transferred to the wells of a 96-well tray. All the experiments were performed using three independent samples. Trays were incubated for four days at 37°C in a 5% CO₂ humid atmosphere. Images of each well were taken using an inverted microscope and OLYMPUS Cell Sens Standard software. To measure the amount of virus able to survive the interaction with the fabric and replicate during those four days in cell culture, RNA was extracted from samples, and after synthesis of the complementary DNA strand (cDNA), a quantitative polymerase chain reaction (qPCR) was performed to determine the number of viral genome copies present in each sample. Briefly, the cell media were removed, and 150 µL of TRI Reagent (Sigma) was used to extract the RNA from each sample, following the manufacturer's instructions. RNA was resuspended in 30 µL ultrapure (nuclease-free) water. For cDNA synthesis, reactions were performed according to the manufacturer's instructions using SuperScript II RT (Invitrogen), 2 µL of RNA, and 250 ng of random primers for each sample. qPCR was performed using a StepOnePlus thermocycler (Thermo Fisher) in 96-well trays. Reactions were always performed in duplicates using GoTaq Master Mix kit (Promega), 2.5 µL of cDNA, and 0.5 µM of each primer per reaction in a final volume of 10 µL. Primers were designed to anneal

to a region of ORF1 of the HCoV-229E genome (PF_NSP12/13, 5'-TGCGGGTATTCTATGCCTGG -3'; PR_NSP12/13, 5'-ACTGGGCAACTTCAAACCTG -3'). Statistical analysis was performed using one-way ANOVA and Bonferroni's post-test, using Microcal Origin 8.5, a statistical tool, and $P < 0.001$ was considered a statistically significant difference.

3.3. Results and discussion

Co_3O_4 QDs were synthesized using tomato pulp and seed extracts (1 g/mL, Carmen variety) at room temperature, as described in the Experimental Section. The synthesis process occurred in three steps, as previously described, which culminate in an olive-green-colored solution (Figure 6A). The progress of the reactions using tomato seed extracts was accompanied by UV-visible spectroscopy (Figure 6B and C, respectively). The absorbance spectra in Figures 6B and C show two bands peaking at 588 and 640 nm, probably due to the formation of $\text{Co}^{\text{(III)}}$ -hydroperoxo organometallic complexes with biomolecules present in the extracts. Similar spectra were obtained for $\text{Co}^{\text{(III)}}$ -hydroperoxo species formed as intermediates of the phenol hydroxylation reaction catalyzed by $\text{Co}^{\text{(II)}}$ complexes with tetradentate ligands (4N) in the presence of hydrogen peroxide (ANANDABABU et al., 2020). The intensity of these ligands to metal charge transfer (LMCT) bands progressively decreased after 2 and 8 days of reaction, as observed for the samples prepared with seeds and pulp, respectively.

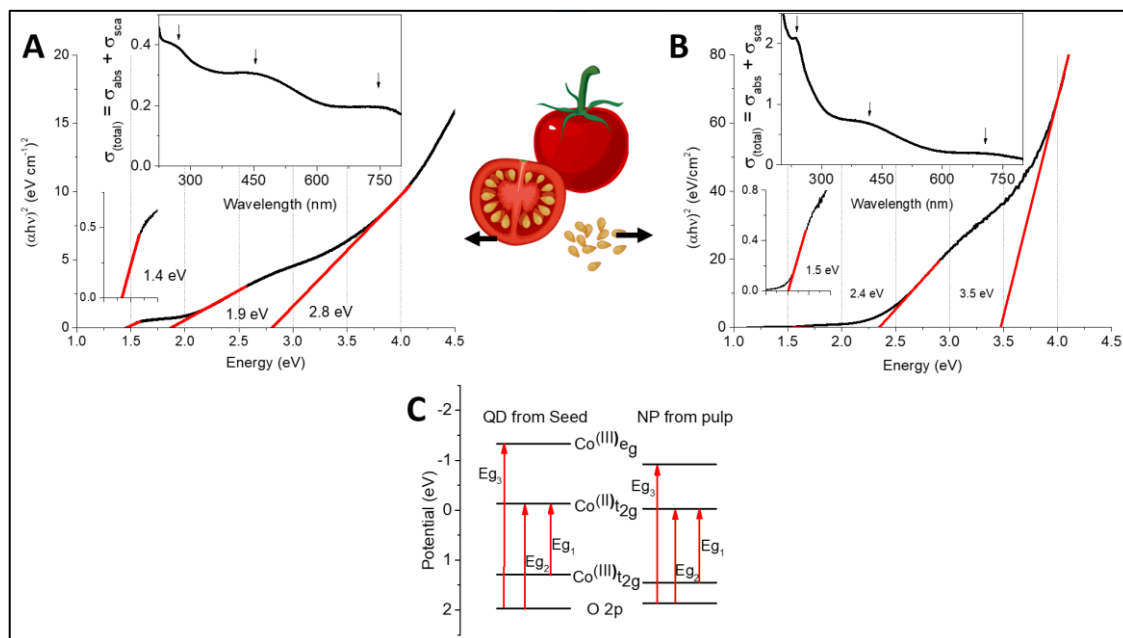
Figure 6. Synthesis of Co_3O_4 QDs using tomato seed extract and cobalt nitrate hexahydrate with high stirring (104 rpm) at room temperature. A) Representative images of tomatoes from Carmen variety. B) Snapshots 1, 2, and 3 show, respectively, the steps of cobalt salt and tomato extract mixing by high stirring, the color change after acidification and high stirring, and the alkalization and high stirring with the appearance of the olive-green color. C) The absorbance spectra obtained immediately after 1 day and 8 days of rest are shown as olive, blue, and yellow-brownish colors, respectively. The inset shows snapshots of the samples at the respective time intervals.



Source: Author

After ~16 days of rest, the samples presented spectral features consistent with the formation of Co_3O_4 bands at around 240, 420, and 700 nm, as indicated by the arrows in the inset of Figure 7B. The bands at 240 and 420 nm are assigned to the ligand-to-metal charge transfer (LMCT) transitions $\text{O}^{2-} \rightarrow \text{Co}^{2+}$, and the band around 700 nm corresponds to the $\text{O}^{2-} \rightarrow \text{Co}^{3+}$ transition (MAKHLOUF et al., 2013). A similar spectrum was obtained for the synthesis of tomato pulp (Figure 7A).

Figure 7. UV-visible spectra of Co_3O_4 QDs and the corresponding Tauc plots. A) UV-spectrum and Tauc plot obtained for Co_3O_4 prepared with tomato pulp. B) UV-spectrum and Tauc plot obtained for Co_3O_4 prepared with tomato seeds. C) Energy diagram for Co_3O_4 nanoparticles obtained with pulp and seeds.



Source: Author

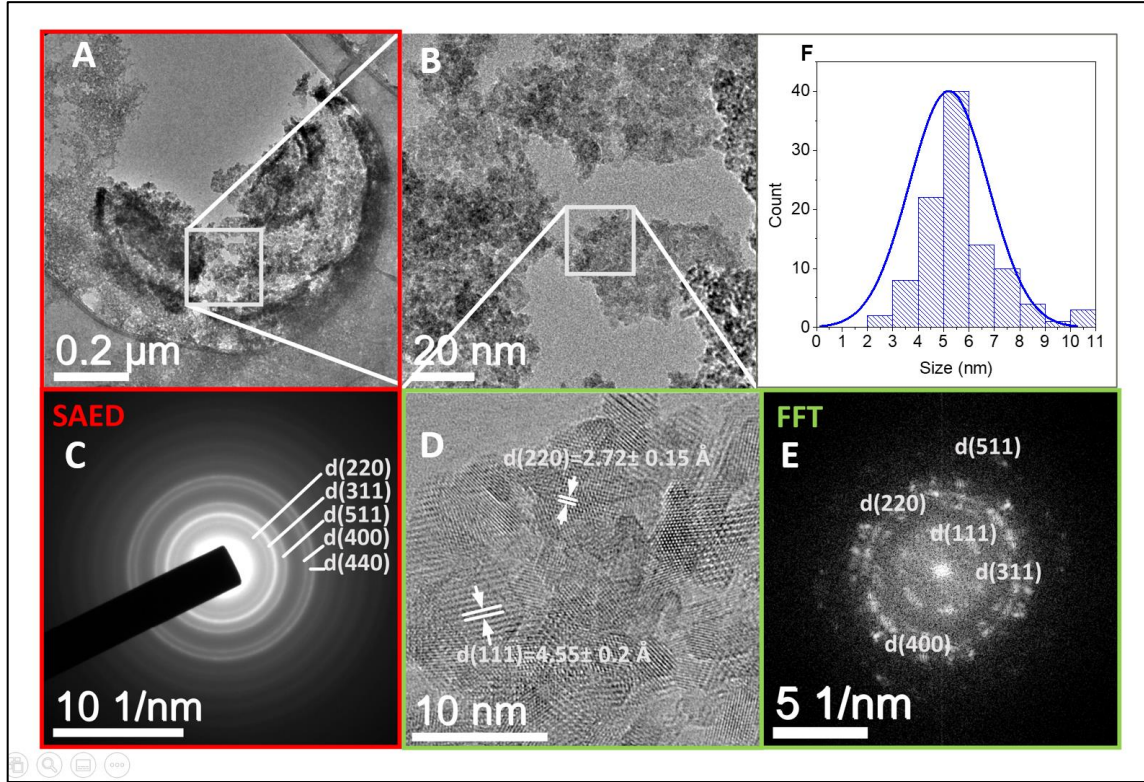
The UV-visible spectra (Figures 7A and B) were used to determine the direct band gap energies using the Tauc plot (insets of Figures 7A and B). The insets of Figure 7A and B show the plots of $(\alpha h\nu)^2$ vs. photo energy (eV) based on the respective UV-visible spectra. The band gap energies intersect with the photon energy ($h\nu$) axis from the extrapolation of the optical absorption coefficient to zero. The band gap energies obtained for Co_3O_4 synthesized using pulp extract are 1.8 and 2.7 eV whereas for the synthesis carried out with seed extracts are 2.4 and 3.5 eV. These values result in band gap energy differences ($\Delta E = E_{g1} - E_{g2}$) of 0.9 and 1.1 eV, respectively for pulp and seed-assisted synthesis. The value of 1.15 eV is close to that obtained for Co_3O_4 QDs synthesized with $\text{CoCl}_2 \cdot 6\text{H}_2\text{O}$ and NaOH in ethanol (XUE et al., 2016). Figure C is the transition, shows Eg (energy diagram), which is the energy it needs to move the electron from one place to another.

For the synthesis using tomato pulp, the optical bandgap energy difference of 0.9 eV is close to the value (0.87 eV) obtained for spherical Co_3O_4 nanoparticles with a mean diameter of 30 nm (DEORI et al., 2013). The higher band gap energy difference exhibited by QDs is due to quantum confinement (DEORI et al., 2013). The Co_3O_4 QDs obtained with tomato

pulp extracts have low colloidal stability due to aggregation and a high content of associated organic material. Therefore, these samples were subjected to calcination at 500°C in an air atmosphere for the acquisition of FESEM images, which corroborated the formation of spherical nanoparticles. It is important to consider that calcination might contribute to an increase in grain size.

For the Co_3O_4 QDs obtained with seeds, only three cycles of washing were sufficient for the acquisition of high-resolution transmission electron microscopy (HRTEM) images without calcination, which corroborated the formation of spinel Co_3O_4 QDs (Figure 8). Figure 8A shows a large area with many Co_3O_4 QDs, which can be better visualized in figure 8B, corresponding to a four-time zoom of the white box. Figure 8D shows HRTEM of the area marked with white box and the average size observed is around 4.5 nm, which is confirmed in figure 8F. Figure 8C shows the SAED pattern obtained from the area shown in Figure 8A, which shows rings corresponding to the (220), (311), (511), (400), and (440) planes of the normal spinel structure of Co_3O_4 . The areas framed in white were magnified, resulting in the image framed in green that was used for the FFT analysis. The panels framed in green show the FFT pattern obtained from figure 8D and show spots of planes (220), (311), (511), and (400) planes of Co_3O_4 .

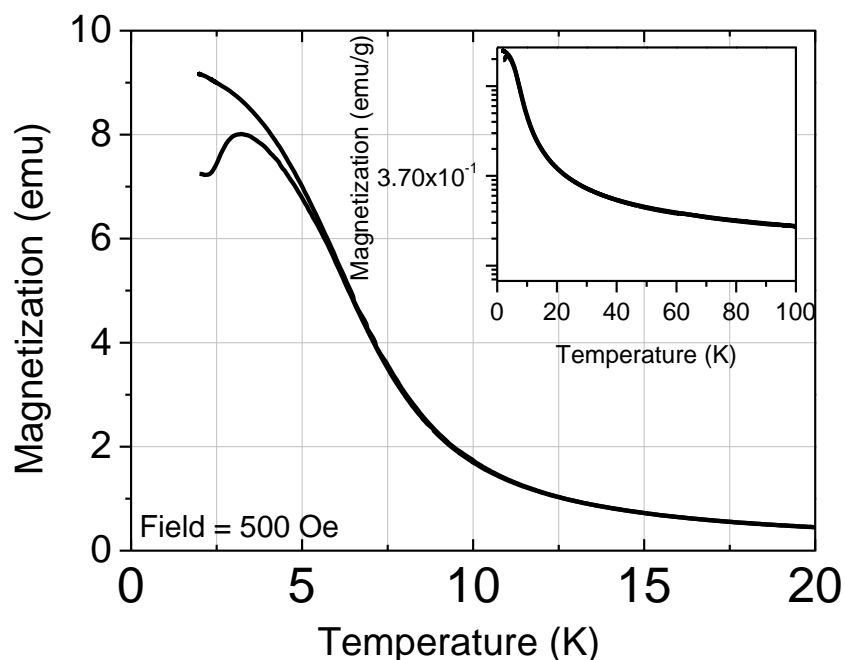
Figure 8. High-resolution transmission electron microscopy (HRTEM) of Co_3O_4 QDs. A) Low magnification image of Co_3O_4 QDs area. B) Four times zoom of the white area in figure 3B. C) SAED of figure 3A showing ring correspondents to planes (220), (311), (511), (400), and (440). D) Four times zoom of the white area in figure 3B. E) Fast Fourier Transform image obtained from figure 3D which also shows spots of planes (220), (311), (511), (400), and (440). F) Histogram of Co_3O_4 QDs with the mean diameter determined as 4.5 ± 0.5 nm.



Source: Author

Figure 9 shows the overlapping of the ZFC and FC curves in the temperature range of 2-100 K. The overlapped ZFC and FC curves are consistent with the superparamagnetic regime, in which thermal fluctuations are dominant over the magnetic anisotropy of the nanostructures (TAKADA et al., 2001). The ZFC and FC curves split at 6.5 K, which is the temperature of irreversibility. The distribution of blocking temperatures (TB) of QDs is assigned from the peak at 3.2 K in the ZFC curve. The TB of approximately 3.0 K is in accordance with previous results obtained by Takada et al. for Co_3O_4 nanocrystals with a 3 nm diameter synthesized in MCM-41 (TAKADA et al., 2001).

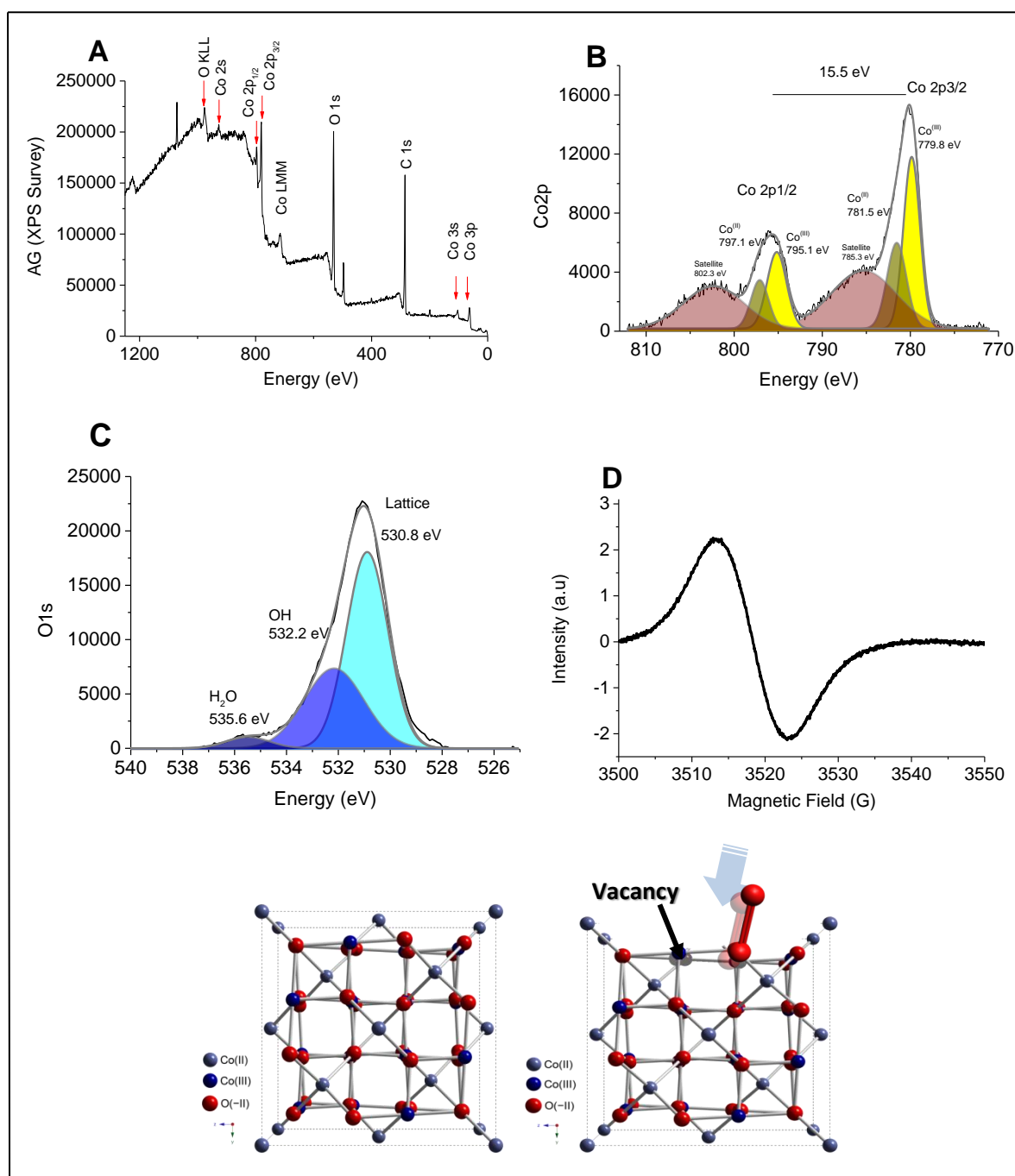
Figure 9. ZFC and FC curves of Co_3O_4 QDs in the temperature range of 2-20 K on a linear scale. The inset shows the ZFC and FC curves in the temperature range of 2-100K with the intensity on a logarithmic scale.

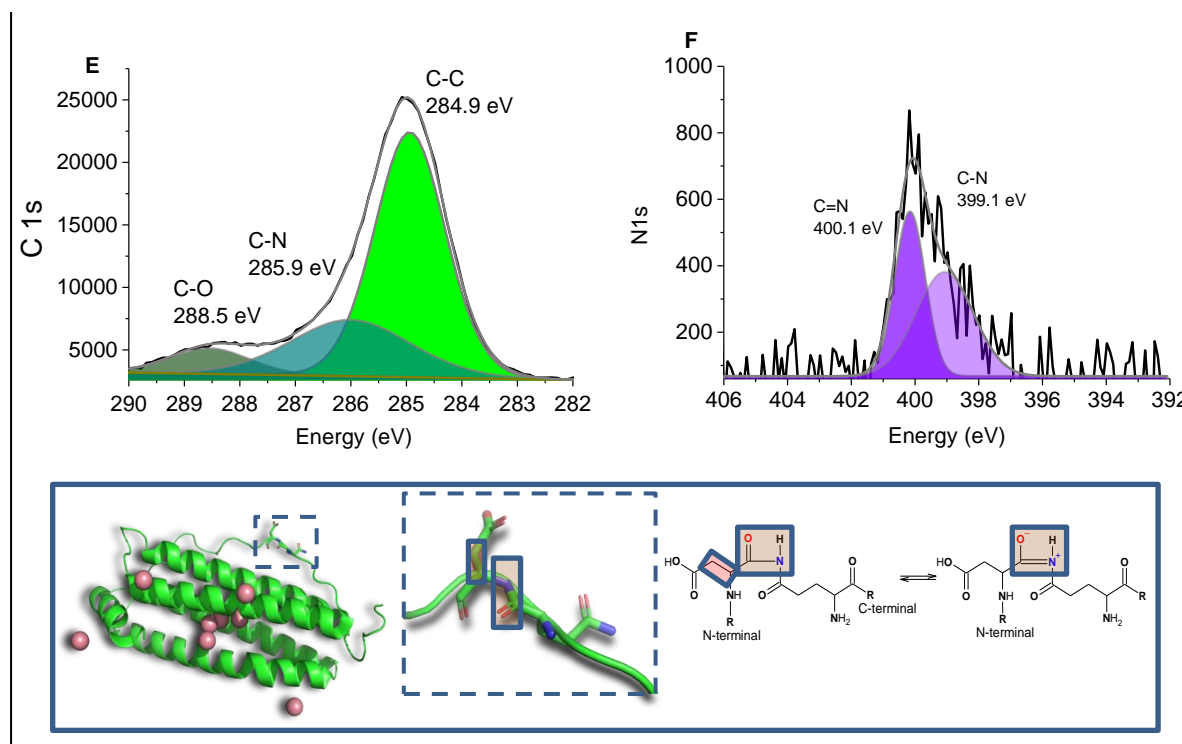


Source: Author

Although the HRTEM data corroborated the formation of Co_3O_4 QDs, it is important to characterize the QD surface chemistry because the synthesis was assisted by tomato biomolecules that probably remained in the material as capping agents. The Co_3O_4 QDs were characterized using SQUID and XPS. X-ray photoelectron spectroscopy (XPS) associated with EPR was used to study the surface chemistry and oxidation state of the metal in the QD samples. Figure 10 shows the XPS spectra of Co_3O_4 QDs. This technique was used to efficiently characterize Co_3O_4 (CAI et al., 2021; LIENAU et al., 2020; TORRES; PALACIO; LÓPEZ, 2021). Figure 10A shows the Al $K\alpha$ XPS survey spectrum, which exhibits the characteristic binding energy regions of Co 2s, Co $2p_{1/2}$, Co $2p_{3/2}$, O 1s, C 1s, Co 3s, and Co 3p at 927, 797, 781, 531, 284.8, 104.9, and 64 eV, respectively.

Figure 10. XPS spectrum of Co_3O_4 QDs. A) XPS survey spectrum. B) and C) high-resolution XPS spectrum of Co 2p and O 1s, respectively. The decomposition of Co 2p_{1/2} and Co 2p_{3/2} bands show the contributions of $\text{Co}^{(\text{III})}$ at 779.8 and 795.1 eV and $\text{Co}^{(\text{II})}$ at 781.5 and 797.1 eV. The decomposition of O 1s spectrum shows the contributions of oxygen in crystal lattice at 530.8 eV, hydroxyl group OH at 532.2, and chemisorbed water at 535.6 eV. D) EPR spectrum of Co_3O_4 QDs at room temperature shows interstitial $\text{Co}^{(\text{II})}$ ions, consistent with the presence of oxygen vacancies that are illustrated on the bottom of the spectrum. E) C 1s spectrum of Co_3O_4 showing the contributions of C-N and C-C BEs at 285.9 and 284.9 eV, respectively, and adventitious carbon at 288.5 eV. F) N 1s BEs of 400.1 and 399.1 assigned to C=N and C-N. The inset shows a ferritin peptide chain with a zoom in a peptide bond sided by the resonance of peptide bonds contributing to the presence of C=N and C-N BEs.





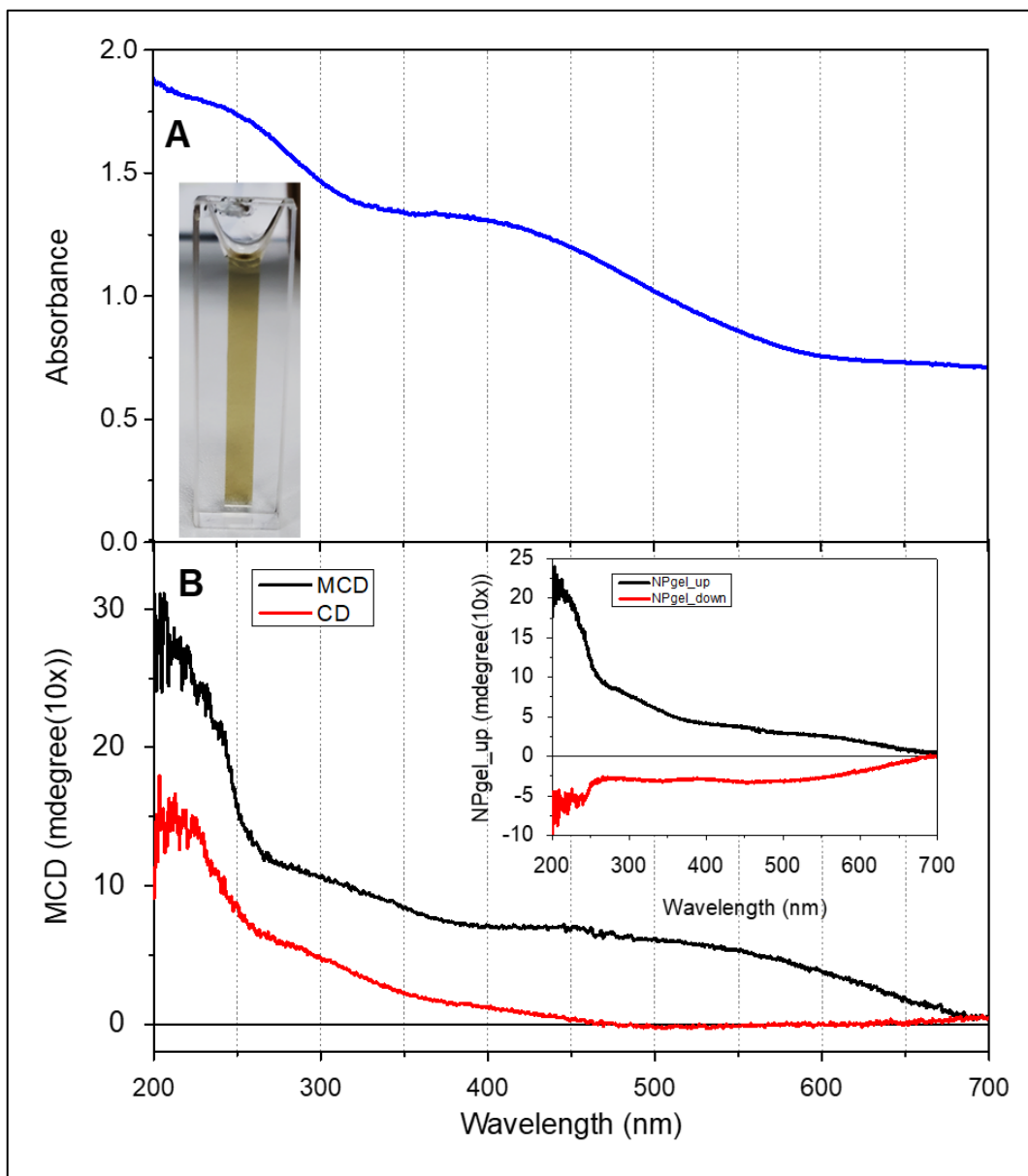
Source: Author

The high-resolution XPS spectrum of Co 2p regions presents doublet binding energies of 780.2 and 795.8 eV, respectively, which arise from the spin-orbit coupling (2p_{3/2} and 2p_{1/2}) with a splitting of 15.5 eV (Fig. 10B). The Co 2p_{1/2} and Co 2p_{3/2} bands were decomposed in contributions of Co^(III) at 779.8 and 795.1 eV and Co^(II) at 781.5 and 797.1 eV. In the Co 2p spectrum, there are no contributions at 778 eV, indicating the absence of metallic Co. The spectrum also shows the shake-up satellite peaks for Co 2p_{1/2} and Co 2p_{3/2} at 802.3 eV and 785 eV, respectively. These bands are attributed to Co^(II) in the presence of oxygen vacancies on the surface, whereas the QD core is a Co₃O₄ crystal. EPR analysis was also used to investigate the oxygen vacancies in the Co₃O₄ QDs (Figure 10D). This technique has been used as an effective tool for examining unpaired electrons in Co₃O₄ (DEORI et al., 2013; TAKADA et al., 2001). The high-intensity EPR spectrum of the paramagnetic phase exhibited by Co₃O₄ confirms that Co^(II) ions are more abundant in the material surface than in the Co₃O₄ crystal, resulting in the presence of oxygen vacancies, illustrated by the crystal structures on the bottom of panels C and D, showing a crystal structure with and without oxygen vacancies (DEORI et al., 2013; TAKADA et al., 2001). The O 1s spectrum shows the contributions of oxygen in the crystal lattice with BE = 530.8 eV, hydroxyl group OH at 532.2, and chemisorbed water at the Co₃O₄ surface (BE = 535.6 eV) (BENKOULA et al., 2015). The C 1s spectrum is consistent with the presence of organic molecules such as proteins on the

Co_3O_4 surface because of the contributions of C-N and C-C BEs at 285.9 eV and 284.9 eV, respectively, and adventitious carbon at 288.5 eV. Adventitious carbon can also contribute to the BE of C-C; however, the presence of peptides on the Co_3O_4 surface is reinforced by the N 1s BEs of 400.1 and 399.1 eV assigned to C=N and C-N, which results from the resonance of the peptide ligation shown in the inset. The formation of Co_3O_4 QDs assisted by tomato seed extract suggests the presence of biomolecules that provide templates for 3D confinement. In addition, the ligands from tomato extract may have massively contributed to the stability and colloidal solubility of the system, controlling the morphology and particle size distribution, and even maintaining the photophysical characteristics of the QDs in aqueous media. Considering that tomato plants have iron content stored in ferritin (AMBE, 1989), this macromolecule is known to be able to provide a nanocage to confine and direct crystal growth, which is a probable bio-template for Co_3O_4 QD synthesis. Previously, we demonstrated by EPR analysis that tomatoes of the Carmen variety present a high content of holoferritin that can provide the formation of nanoparticulated magnetite, whereas cherry tomatoes have a low content of this protein (TOFANELLO et al., 2021a).

Considering that crystal growth possibly occurred in association with chiral molecules such as ferritin chains, the presence of CD and MCD signals originating from chiral molecules adsorbed on the material surface and distortion of the crystal structure was investigated by CD and MCD techniques. Figure 11A and B show the absorbance spectra of the Co_3O_4 QDs and the corresponding CD (red line) and MCD (black line) spectra. The CD and MCD spectra were obtained by the sum and subtraction of the signals obtained in the positive and negative field directions (0.86 T), as shown in the inset. For the MCD measurements, the Co_3O_4 QDs were immobilized on a polyacrylamide gel, as shown in the inset of Figure 11A. The presence of an MCD signal in the spectral region in which Co_3O_4 is absorbed is suggestive of chiral distortion of the crystal.

Figure 11. Characterization of chiral Co_3O_4 QDs – CD and MCD. A) Absorbance spectrum of Co_3O_4 QDs with the inset showing a snapshot of the Co_3O_4 QDs immobilized in a polyacrylamide gel. B) Corresponding CD (red line) and MCD (black line) spectra of the immobilized material in a gel.



Source: Author

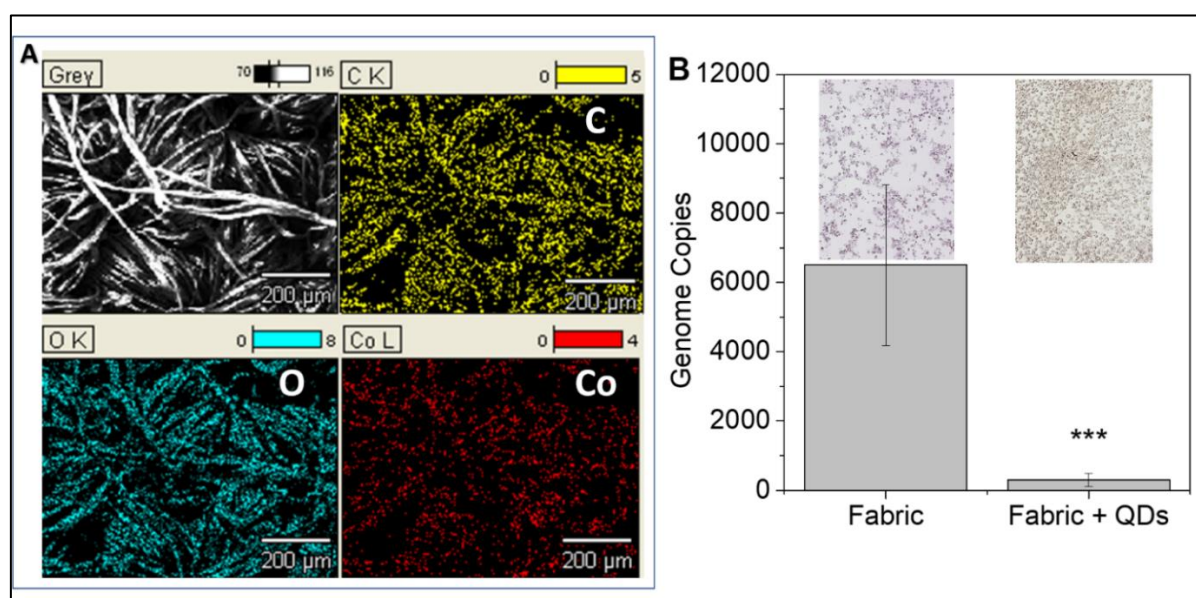
Consistent with the importance of ferritin for the synthesis of Co_3O_4 QDs, this material was also obtained with horse spleen holoferritin using a protocol similar to that used for the synthesis of tomato seeds. The present study and more recent literature data inspired us to investigate the application of chiral nanomaterials for the optical detection of coronavirus, which is ongoing in our laboratories (BENKOULA et al., 2015; YANG et al., 2018; ZHANG et al., 2016). QDs have been used in photocatalysis.(JOUYANDEH et al., 2021; LIU et al.,

2021; RAO et al., 2019; SHI et al., 2020; WANG et al., 2020a; YANG et al., 2020) The presence of Co(II) interstitial and oxygen vacancies indicates that Co_3O_4 QDs are promising materials for the generation of reactive oxygen species (ROS) and photocatalysis to oxidize virus biomolecules. Therefore, the subsequent step was to investigate the possible applications of Co_3O_4 QDs as virucidal agents.

3.3.1. Virucidal activity

QDs have been reported as a promising agent to fight against COVID-19 through three principal mechanisms: interaction with viral envelope components, impairment of virus replication, and virus biosensing by fluorescence (AMBE, 1989; CANTARELLI; REGITANO-D'ARCE; PALMA, 1993; MENEZES et al., 2020). Regarding the interaction with the viral envelope, we can consider direct interactions responsible for Spike protein unfolding and lipid oxidation and indirectly by the generation of reactive oxygen species that attack proteins and lipids of the viral envelope. Considering that the COVID-19 pandemic poses a challenge to the development of smart, sustainable, and protective clothes, the Co_3O_4 QDs were investigated as virucidal agents in textiles.

Figure 12. Antiviral application of Co_3O_4 QDs. A) Representative FESEM-EDX images of cotton fabric impregnated with Co_3O_4 QDs showing the co-localization of carbon (yellow), oxygen (blue), and cobalt (red) elements in the cotton fibers (upper left panel). B) Virucidal activity of QDs. Viral load (genome copies) of Human coronavirus 229E (HCoV-229E) detected by qPCR 4 days post-infection after 5 minutes of incubation to either cotton fabric + QDs or cotton fabric only. A twenty-fold reduction can be detected on virus recovered from cotton fabric + QDs when compared to control fabric only. The inset shows representative images of the MRC-5 cells, using a 100x augment, after 4 days of incubation with the 200 μl of medium recovered from the fabrics. A greater number of live cells can be seen on the right panel, where viruses were incubated with cotton fabric + Co_3O_4 QDs. The statistical analysis was done by One-way ANOVA with Bonferroni's post-test (***: $P < 0.001$).



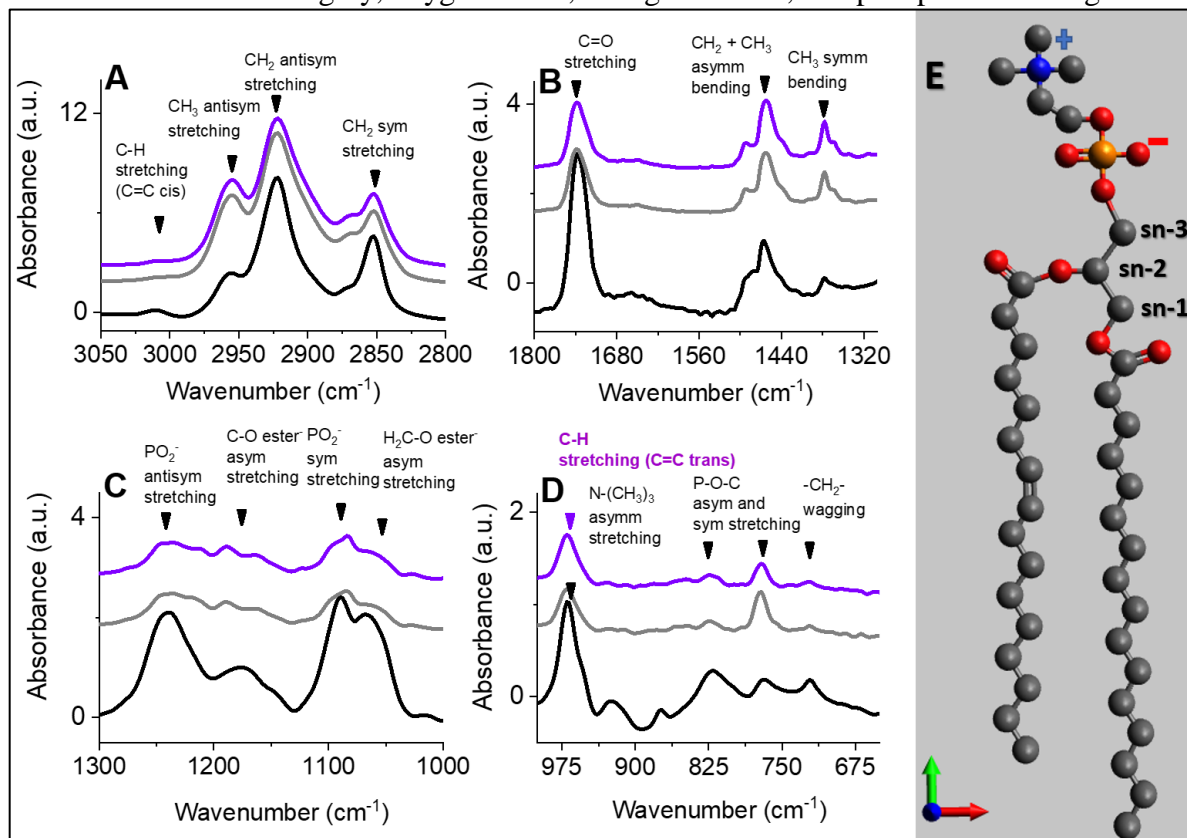
Source: Author

The Co_3O_4 QDs present cost-effective and environmental advantages in relation to the widely used silver nanoparticles and absorption in the visible region of the spectrum, in contrast to TiO_2 and ZnO , which are also largely used as microbicidal agents. For virucidal application, Co_3O_4 was incorporated into the cotton fabric, as described in the Materials and Methods, and characterized by field emission scanning electron microscopy with energy dispersive X-ray analysis (Figure 12A). The Co_3O_4 -modified fabric and its corresponding control (original cotton fabric) were challenged by inoculation with human coronavirus 229E (HCoV-229E) that infects humans. HCoV-229E is an enveloped virus used as a model that can be extrapolated to SARS-CoV-2 because the oxidative damage induced by ROS is non-specific. The fabrics inoculated with HCoV-229E for 5 min were washed with culture medium and transferred into MRC-5 cells in culture.

Viral load (genome copies) of human coronavirus 229E (HCoV-229E) was detected by qPCR 4 days post-infection, and the results are presented in Figure 12B. The cotton fabric impregnated with Co_3O_4 QDs presented a twenty-fold reduction in the recovered virus when compared to the control fabric only. The presence of viable viruses was determined by the number of viral genomes determined by qPCR. The inset shows representative images of MRC-5 cells incubated with inoculum from the original cotton fabric, in which extensive cell lysis is evident as a result of viral infection (left). Cells incubated with the fabric + Co_3O_4 QD inoculum (right) presented lower cell death, demonstrating a lower number of viable viruses recovered from the material. Thus, Co_3O_4 -modified cotton fabrics are potentially useful for the production of self-disinfecting personal equipment protection.

To determine the mechanism by which Co_3O_4 QDs promote the inactivation of enveloped virus HCoV-229E, PC liposomes, as a model of the lipid fraction of the viral envelope, were exposed to the nanomaterial for 10 min in the absence and presence of UV light. Owing to the UV and visible (room illumination) light absorption capacity, the effects of the QDs on the phospholipid were identical under the two illumination conditions. Figure 13 A, B, C, and D show the main spectral changes promoted by the Co_3O_4 QDs on the PC.

Figure 13. FTIR analysis of the effect of Co_3O_4 QDs on phosphatidylcholine. Panels A) to D) show the spectra of PC pristine (black lines) and exposed to Co_3O_4 QDs under visible light (grey lines) and UV light (violet lines). In the spectra, the assignment to the chemical group vibration is indicated by black arrows. The indication of C=C trans vibration is in violet arrow and font. E) Structure of PC with the indication of sn-1, sn-2, and sn-3 positions. The structure was drawn using the open-source molecular builder and visualization tool, Avogadro software. Carbons are in grey, oxygen in red, nitrogen in blue, and phosphate in orange.



Source: Author

In Figure 13A, the decrease in the band at 3010 cm^{-1} is associated with a decrease in the C-H stretching vibration of the *cis*-double bond (C=C) (DAOUD et al., 2019). The frequency of this band was found to be in the range of 3006 and 3009 cm^{-1} according to the different fatty acid compositions and degrees of acyl chain unsaturation. Phospholipid oxidation promotes *cis*-double bond rearrangement to form a *trans*-double bond, leading to a decrease in the band at 3010 cm^{-1} (DAOUD et al., 2019; FINLAYSON-PITTS; SWEETMAN; WEISSBART, 1987). The peaks corresponding to the stretching of C-H hydrocarbon are identified in Figure 13A as C-H stretching of -C=C-H at 3010 cm^{-1} , CH_3 antisymmetric stretch at 2954 cm^{-1} , antisymmetric stretch of CH_2 at 2922 cm^{-1} , and symmetric stretching of CH_2 at 2854 cm^{-1} (DAOUD et al., 2019). Differences in relative intensities were identified in these C-H stretch peaks between native PC and PC exposed to QDs, indicating

that changes occurred in the phospholipid methylene and methyl groups. As shown in Figure 13B, the band peak at 1737 cm^{-1} is attributed to the stretching vibrations of the carbonyl group of glycerol-acyl esters (-C=O) (DAOUD et al., 2019; FINLAYSON-PITTS; SWEETMAN; WEISSBART, 1987). The decrease in this band can be attributed to the cleavage of the carbonyl esters promoted by the QDs. The asymmetric bending of CH_2 and CH_3 vibrations at 1462 cm^{-1} and the symmetric CH_3 bending vibration at 1378 cm^{-1} were also identified (Figure 13B). These bands intensified after PC exposure of the QDs. The intensification of these bands, promoted by lipid oxidation, has been previously reported (DAOUD et al., 2019). In Figure 13C, the intense and broadband at 1240 cm^{-1} , assigned to the asymmetric stretch of PO_2^- ($\nu_a\text{PO}_2^-$) exhibited a significant decrease and splitting with the appearance of peaks at 1247, 1236, and 1213 cm^{-1} . The $\nu_a\text{PO}_2^-$ band is sensitive to the hydration of the phosphate group and PC conformation, indicating reactions with Co_3O_4 QDs that affected the PC head group (POHLE et al., 2001). The ester C-O stretch in the fatty acid acyl chains at the sn-1 and sn-2 positions were identified in native PC by the bands at 1174 and 1148 cm^{-1} , respectively. After exposure to Co_3O_4 QDs, these bands were shifted to 1188 and 1162 cm^{-1} , respectively, which is also consistent with the changes in the PC head group. The broad bands at 1090 cm^{-1} and 1068 cm^{-1} , assigned to C-O and C-O- PO_2 stretches, changed to bands at 1097 and 1083 cm^{-1} with a shoulder at 1062 cm^{-1} , which are also coherent with significant changes in the PC head group. In pristine PC, the intense band at 970 cm^{-1} with a shoulder at 952 cm^{-1} (Figure 8D) is assigned to the $\text{N}^+\text{-CH}_3$ asymmetric stretch, and the bands at 820 and 767 cm^{-1} correspond to P-O-C asymmetric and symmetric stretching, respectively, whereas the band at 720 cm^{-1} is attributed to $\text{-CH}_2\text{-}$ wagging. After exposure to Co_3O_4 QDs, the complex band corresponds to the $\text{N}^+\text{-CH}_3$ asymmetric stretch (970 cm^{-1}) was replaced by a symmetric low-intensity band peaking at 971 cm^{-1} . Considering the decrease in the C-H stretching vibration of the *cis*-double bond (C=C) observed after PC exposure to Co_3O_4 QDs (Figure 13A), the appearance of the band at 971 cm^{-1} can be assigned to the contribution of the trans isomer (DAOUD et al., 2019; PAES DE BARROS et al., 2020). The Co_3O_4 QDs also significantly decreased the intensity of the P-O-C asymmetric stretch and $\text{-CH}_2\text{-}$ wagging. Therefore, changes in the lipid fraction of the viral envelope can be postulated as a mechanism of viral inactivation in textiles modified with Co_3O_4 QDs, which does not exclude additional damage to the protein fraction of the virus. The damage can result from the attack of ROS and direct reaction with the material due to the presence of oxygen vacancies.

3.4. Conclusion

Multifunctional Co_3O_4 QDs were synthesized from cobalt nitrate using tomato seed extract as a source of reducing and template agents at room temperature without the use of solvents. Tomato ferritin is postulated as the main template for the 3D confined growth of Co_3O_4 nanocrystals with chiral distortion. Accordingly, purified horse spleen ferritin was equally efficient for synthesizing Co_3O_4 QDs. The presence of $\text{Co}^{(\text{II})}$ interstitial and oxygen vacancies provided reactivity for Co_3O_4 QDs, making it possible to apply the nanostructures as virucidal agents in cotton fabrics.

4. CHAPTER 2

DEGRADATION OF CIPROFLOXACIN BY GREEN COBALT OXIDE QUANTUM DOTS

Authors: Julia D. Bronzato, Juliana D. Bronzato, Adrianne M. M. Brito, Jefferson Bettini, Maicon R. Z. Passini, Brenda P. F. A. Gomes and Iseli L. Nantes-Cardoso.

Periodic: Applied Surface Science, Volume 609, 30 January 2023, 155193.

Publication Date: Received 10 May 2022, Revised 17 September 2022, Accepted 1 October 2022, Available online 17 October 2022, Version of Record 20 October 2022.

ABSTRACT – Ciprofloxacin (CIPRO) is a fluoroquinolone antibiotic extensively used to treat various bacterial infections. The extensive use of CIPRO has promoted its accumulation in diverse aquatic environments as an emergent pollutant. Concentrations of CIPRO found in surface and ground waters and seas vary from ng to mg/L and represent a real risk for the rise of new resistant bacterial strains. The complex and stable chemical CIPRO structure is not favorable for biological degradation. However, magnetic Co_3O_4 quantum dots (Co_3O_4 QDs) with 5 nm of mean diameter synthesized using biomolecules from tomato (*Solanum Lycopersicum* L.) seed extract were efficient to promote photodegradation of this emergent pollutant under UV irradiation. CIPRO degradation was corroborated by UV-visible and Fourier Transform Infrared (FTIR) spectrophotometry. The photodegradation using UV-light in the presence of Co_3O_4 QDs was the more efficient strategy to impair the bactericidal action of CIPRO and, consequently, to avoid the development of bacteria-resistant strains. The Co_3O_4 QDs are a low-cost, efficient, and green option for CIPRO degradation.

4.1. Introduction

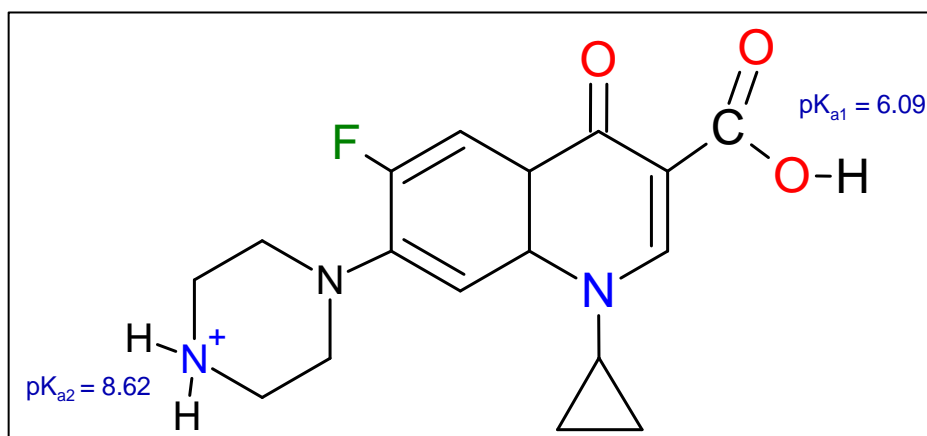
Semiconductors have received significant attention for the degradation of organic compounds because of their catalytic and photocatalytic properties (BAI; LIU; SUN, 2011; BEEGAM et al., 2016; LI et al., 2020; TOFANELLO et al., 2021b; YADAV et al., 2022; ZHAO et al., 2018; ZHENG et al., 2015). Semiconductors containing oxygen vacancies in their crystal lattice are highly efficient in degrading organic compounds (GANHARUL et al., 2021). Metal oxide semiconductors and their doped variants can generate reactive oxygen species such as hydroxyl radicals ($\bullet\text{OH}$), superoxide ions ($\text{O}_2^{\bullet-}$), hydrogen peroxide (H_2O_2), and singlet oxygen ($^1\Delta_g\text{O}_2$) (AMETA et al., 2018; BESSEGATO et al., 2015; GANHARUL et al., 2021; MENEZES et al., 2020; NOSAKA; NOSAKA, 2016). These materials submitted to irradiation exhibit charge separation, leading to ROS generation used to degrade the organic compound through advanced oxidation processes (AOPs) (AMETA et al., 2018). Other processes such as nano etching combined with photochemical properties can also contribute to CIPRO photodegradation (TOFANELLO et al., 2021b). The use of green and low-cost methods to develop nanoparticles, such as plant and biomolecule-based, is currently present in the research field (KOMBAIAH et al., 2019). Some other synthesis routes are toxic, expensive, and require calcination processes (FARHADI; JAVANMARD; NADRI, 2016). Therefore, this is a field of constant improvement and development.

Emerging pollutants comprise synthetic and natural chemical compounds that accumulate in the environment from different sources. They represent a serious problem for the environment and animal and human health (ABDULRAZAQ et al., 2021; FERRER; ZWEIGENBAUM; THURMAN, 2010). Significant sources of emergent pollutants are pesticides, consumer and industrial waste products, personal care products, illicit drugs, and pharmaceuticals (ABDULRAZAQ et al., 2021; FERRER; ZWEIGENBAUM; THURMAN, 2010). Antibiotics have been widely used for human and animal therapies, aquaculture, and crop fields (RODRIGUEZ-MOZAZ et al., 2015). However, conventional wastewater treatment plants cannot treat it properly (KARTHIKEYAN; MEYER, 2006). Consequently, it contaminates the water we drink and the soil we plant, and it turns into an endless cycle (AWAD et al., 2013), leading to new resistant bacteria (JIMÉNEZ-TOTOTZINTLE et al., 2018). A few alternatives have been developed to treat this harmful antibiotic before releasing it to nature, such as biological, physical, and chemical degradation treatment (YANG et al., 2021), that are either expensive or cause even more pollutants (MAKOFANE; MOTAUNG; HINTSHO-MBITA, 2021). Among the pharmaceuticals included in the list of emergent

pollutants, the third-generation fluoroquinolone antibiotic ciprofloxacin (CIPRO) deserves consideration due to its widespread use to combat a wide variety of bacterial infections (FRADE et al., 2014; YU et al., 2019). CIPRO residues, in the concentration range from ng to mg/L (MUTHUMARIAPPAN, 2013), have been found in water sources (WANG; WANG; YANG, 2018) agricultural and home wastes (YU et al., 2019; ZHANG et al., 2015).

CIPRO presents a complex and stable chemical structure (Figure 14) that is unfavorable for biological decomposition (LIAO et al., 2016).

Figure 14. CIPRO chemical structure with its ionizable groups with respective pK_a values.



Source: Author

CIPRO exhibits photochemical properties due to the quinolone moiety (BANI-YASEEN et al., 2013). The occurrence of electronically excited states of CIPRO is responsible for photosensitivity in patients (CUQUERELLA et al., 2012; LORENZO; NAVARATNAM; ALLEN, 2008) photodegradation in diverse environments subjected to light irradiation (GUO et al., 2013a; KIM et al., 2020). Researchers have dedicated crescent efforts to develop effective CIPRO removal and degradation methodologies. Photocatalysis is a promising solution for the degradation of the residues of antibiotics in the aquatic environment, and it is one of the most used methods for this proposal (HARIHARAN, 2006). The present study concerned the synthesis of Co_3O_4 quantum dots and their applicability in the degradation of the emergent pollutant CIPRO, a significant environmental challenge.

4.2. Material and methods

4.2.1. Chemicals

Cobalt (II) nitrate hexahydrate ($\text{Co}(\text{NO}_3)_2 \cdot 6\text{H}_2\text{O}$) was purchased from Sigma-Aldrich Corp. (St. Louis, MO, USA). Ciprofloxacin hydrochloride salt (500 mg), the soluble form used in clinical applications, is commercially available. “Carmen” variety tomatoes were purchased at the local market in Santo André, SP, Brazil.

4.2.2. Synthesis and characterization of Co_3O_4 quantum dots produced with tomato seed extracts

Co_3O_4 quantum dots were synthesized using the biomolecules of tomato seed extracts as reducing agents and templates for the cobalt oxide crystal growing from cobalt(II) nitrate as previously published (BRONZATO et al., 2022). Briefly, the synthesis was conducted at room temperature, using the UltraTurrax to homogenize tomato seed extract and cobalt salt. The cobalt (II) nitrate hexahydrate ($\text{Co}(\text{NO}_3)_2 \cdot 6\text{H}_2\text{O}$) was mixed with a solution of tomato seed extract, not filtered, and Milli-Q water. After this first homogenization step, the mixture was acidified with HCl 1M, pH 2. Lastly, the solution was alkalized with NaOH 10M, reaching pH 12. Throughout the process, the mixture was kept under stirring at 10,000 rpm. The final solution was then kept in a glass Becker, and after approximately 16 days, it turned into a dark brown color, and the UV-visible spectroscopy showed bands compatible with the formation of the Co_3O_4 QDs. After synthesis, Co_3O_4 Quantum Dots were submitted to dialysis and characterized by high-resolution transmission electron microscopy (HRTEM), XPS, and EPR as previously published (BRONZATO et al., 2022). The preparation for the analysis and application for CIPRO degradation was preceded by triple washing and resuspension in Milli-Q water. For the use in CIPRO photodegradation, the Co_3O_4 QDs had the protein corona removed by the enzyme proteinase K. Proteinase K was used in a concentration of 400 nM. The washed solution of QDs was adjusted to pH 6 with NaOH 1M, then mixed for 24 hours using a stirrer and dialyzed in a constant stirring with Milli-Q water for 2 hours (HOSSEINI-KOUPAEI et al., 2019).

4.2.3. UV-visible spectroscopy

UV-visible spectroscopy was carried out using a Varian Cary 50 UV-Visible that operates in the range of 190 to 1100 nm with intervals (resolution) of 1 nm. This technique was used to accompany the synthesis of Co_3O_4 quantum dots and the photodegradation of CIPRO. Different spectral ranges were selected according to the sample to be analyzed.

4.2.4. FTIR spectroscopy

In-situ analysis of CIPRO degradation was analyzed by attenuated total reflectance-Fourier transform infrared (ATR-FTIR) technique to identify changes in the functional groups of CIPRO molecule. The infrared spectra were run in a Varian 640-IR Spectrometer. The data were fitted with a DLaTGS detector and a PIKE MIRacle™ single reflection horizontal ATR accessory with a crystal diamond with ~1.8 mm of sampling area using an angle of 45 degrees for light incidence. The samples were dropped on the diamond crystal surface and were slowly dried by the proximity of silica particles. The spectra were calculated from 64 scans at 4 cm^{-1} resolution using air as the reference. The specific software of the spectrometer (Varian Resolutions Pro software program). The peaks were analyzed and compared after a vector normalization of each spectrum using the Origin Pro 8 (OriginLab Corp., USA) software program.

4.2.5. Application of Co_3O_4 QDs for CIPRO photodegradation

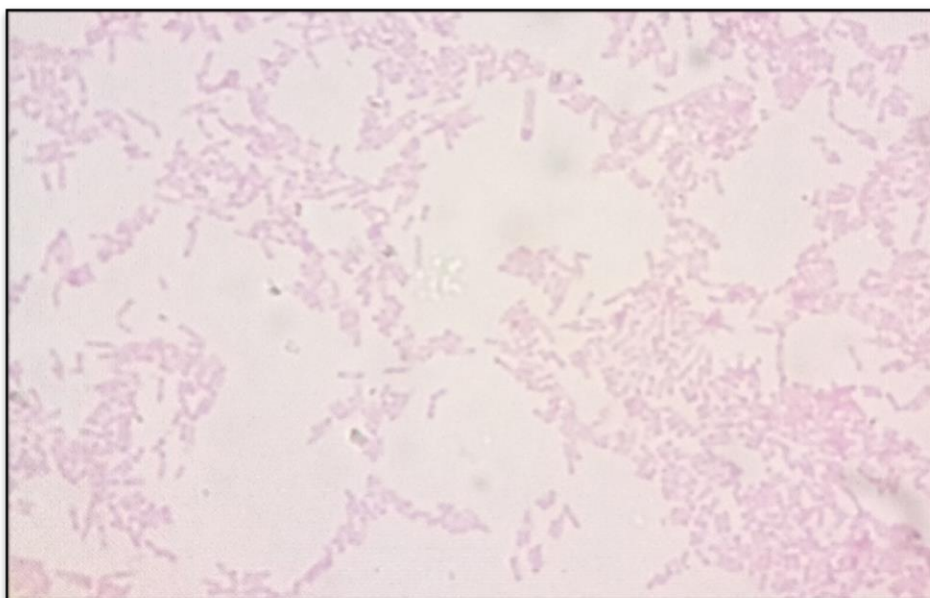
The photocatalytic degradation of CIPRO was performed using 0.008 mg of the photocatalyst in 100 mL of CIPRO solution (0.02 mg/mL) in deionized water. Before illumination, the sample containing the antibiotic and Co_3O_4 QDs was maintained in the dark for at least 15 min to guarantee the establishment of adsorption-desorption equilibrium. The samples were irradiated with a UV lamp at a fixed wavelength ($\lambda = 254\text{ nm}$) at $25\text{ }^\circ\text{C}$ in deionized water. A compact 4 W UVB lamp (UVGL-25 model, UVP Company, Upland, CA, USA) was used to photosensitize the samples. The incident light intensity was determined at 4 mW cm^{-2} , measured by a laser power meter model FieldMate with PowerMax thermal sensors at a distance of 4 cm (SANTOS et al., 2020). The irradiation with solar simulator used the MiniSol model LSH-7320 of a class ABA LED-based Solar Simulator with a 2-inch x 2-

inch illumination area. The degradation was monitored using UV-Vis spectroscopy at time intervals of 5, 15, 25, and 60 min in the 800–200 nm range. Photobleaching was analyzed by the temporal decrease in the absorbance bands and the differential spectra obtained by subtracting the final from the initial spectra.

4.2.6. Microbiological tests

Escherichia coli ATCC 25922 was used for microbiological analysis. Colonies were previously subcultured in appropriate culture media and under gaseous conditions to confirm their purity through catalase and Gram-morphology tests before each experiment (Figure 15).

Figure 145. E.coli in Gram stain showing Gram-negative bacilli. 100x optical microscopy.



Source: Author

4.2.7. Etest

The susceptibility of *E. coli* isolates by ciprofloxacin was determined by using the Etest method (BioMérieux SA, Marcy-l'Etoile, France) according to the reference (CERCENADO et al., 2007). Colonies were suspended in BHI media to achieve a 1.0 McFarland turbidity standard density. A cotton wool swab soaked in the inoculum was used to inoculate the surface of BHI agar plates. The Etest strip was applied to the plate, and its

antibiotic concentration varied from 0.002-32 $\mu\text{g/ml}$. The plates were immediately incubated at 37°C and read after 24 hours.

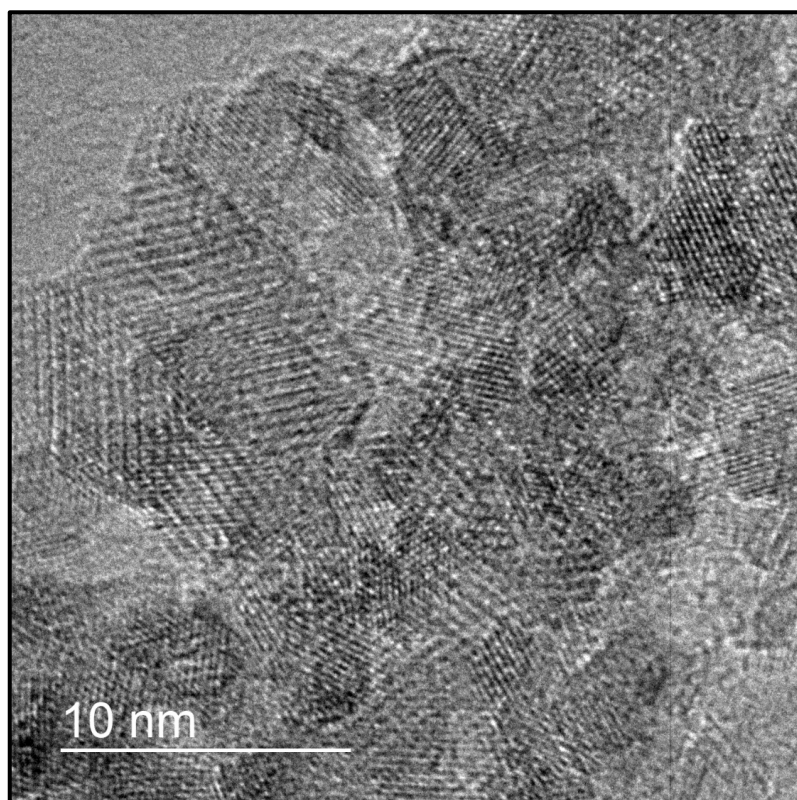
4.2.8. Agar diffusion test

The methodology used was adapted from literature (European Committee for Antimicrobial Susceptibility Testing (EUCAST) of the European Society of Clinical Microbiology and Infectious Diseases (ESCMID), 2000; Gomes et al., 2002; Parvekar et al., 2020). After overnight growth of *E. coli* in BHI agar, colonies were inoculated into tubes containing BHI media. The suspension was adjusted spectrophotometrically at 800 nm to match the transmittance of 90 % and poured onto 140-mm plates containing a previously set layer of Mueller Hinton agar. Sterile stainless-steel tubes (8.0 x 1.0 x 10 mm; inner diameter, 6 mm) were added to the surfaces of the agar plates and filled with 50 μl of each substance to be tested. The plates were kept for 2 hours at room temperature to allow the diffusion of the substances through the agar and then incubated at 37°C under appropriate gaseous conditions for 24 hours. Zones of inhibition of microbial growth were measured with a digital pachymeter and recorded. The test was done in triplicate.

4.3. Results and discussion

Co_3O_4 QDs were synthesized using tomato seed extract at room temperature and characterized by different techniques (BRONZATO et al., 2022), including HRTEM.

Figure 156. High-resolution transmission electron microscopy (HRTEM) of the QDs.



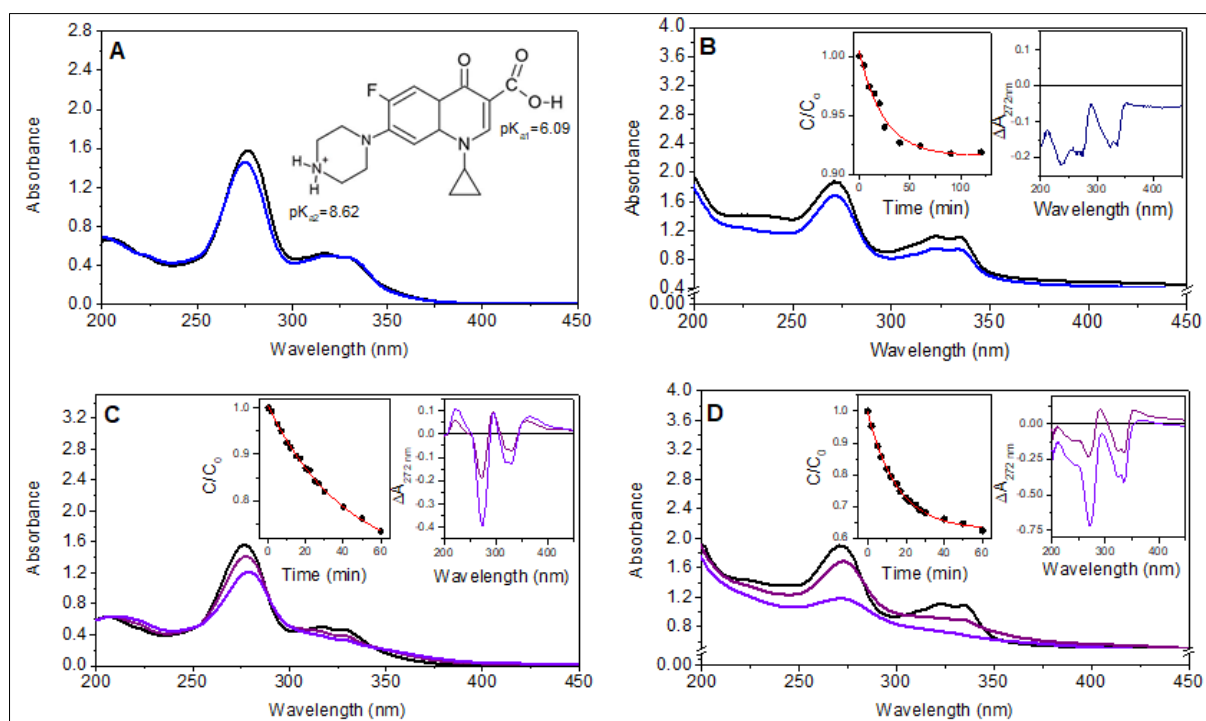
Source: CNPEM

Figure 16 shows a representative image of Co_3O_4 QDs average size observed is around 4.5 nm. From these images, SAED and FTT patterns determined crystalline planes corresponding to the spinel structure of Co_3O_4 (BRONZATO et al., 2022), in other words, normal structure with octahedrally coordinated Co^{3+} and tetrahedrally coordinated Co^{2+} . Considering that Co_3O_4 QDs present $\text{Co}^{(\text{II})}$ interstitial sustaining the presence of oxygen vacancies (ZHANG et al., 2016) and exhibited a virucidal action when incorporated in fabrics due to the generation of ROS, in this study, it was used to promote photocatalytic degradation of the emergent pollutant CIPRO.

Inorganic nanostructured materials are attractive for application in photocatalysis because of their stability, high performance, and possible molecular selectivity. Nanostructured materials provide more significant surface areas and tunability of the electronic states. Furthermore, other characteristics such as oxygen vacancies can contribute to an efficient application in photodegradation, because of the crystal structure defects, which

result in a lack of oxygen in the network and O_2 gets in, these vacancies are important to generate reactive species. Here, the emergent pollutant CIPRO is a fluoroquinolone antibiotic extensively used to treat a variety of bacterial infections, such as urinal infections (SHARMA et al., 2010). The extensive use of Cipro has promoted its accumulation in diverse aquatic environments as an emergent pollutant (CLEUVERS, 2005; FRADE et al., 2014; YU et al., 2019). Cipro was elected for checking the photocatalytic performance of Co_3O_4 QDs (EDVINSSON, 2018). Concentrations of this antibiotic found in surface and ground waters, as well as in seas, vary from ng to mg/L^{-1} and represent a real risk for the rise of new resistant bacterial strains (MUTHUMARIAPPAN, 2013). An interesting strategy for Cipro degradation is semiconductors with the capacity to produce ROS under illumination (BEEGAM et al., 2016; DONG et al., 2015; LIU; WANG; WANG, 2020). Figure 17A shows the Cipro spectra before and after 3 h of irradiation with a simulator of the sun emission in the visible and near-infrared spectral ranges (400-750 and 750-1100 nm, respectively) that are not absorbed by this antibiotic.

Figure 167. Changes in Cipro spectrum during exposure to a solar simulator and UV light in the absence and presence of Co_3O_4 QDs. A) Spectral changes of Cipro before and after 3 h of exposure to a solar simulator emitting from 400-1100 nm. The inset shows the Cipro structure with the pK_a values $\text{pK}_{a1} = 6.09$ and $\text{pK}_{a2} = 8.62$, resulting in an isoelectric point (pI) of 7.14 (CAÇO et al., 2008). B) Spectral changes of Cipro associated to Co_3O_4 QDs before and after 3 h of exposure to a solar simulator emitting from 400-1100 nm. The insets show the C/ C_0 curve of photobleaching monitored at 272 nm and the differential spectrum obtained by subtracting the spectrum of pristine Cipro from the spectrum obtained after 3 h of irradiation. C) Spectral changes of Cipro before and after 1 h of exposure to UV light source. The insets show the C/ C_0 curve of photobleaching monitored at 272 nm and the differential spectrum obtained as described above. D) Spectral changes of Cipro associated with Co_3O_4 QDs before and after 1 h of exposure to UV light source. The insets show the C/ C_0 curve of photobleaching monitored at 272 nm and the differential spectrum obtained as described above.



Source: Author

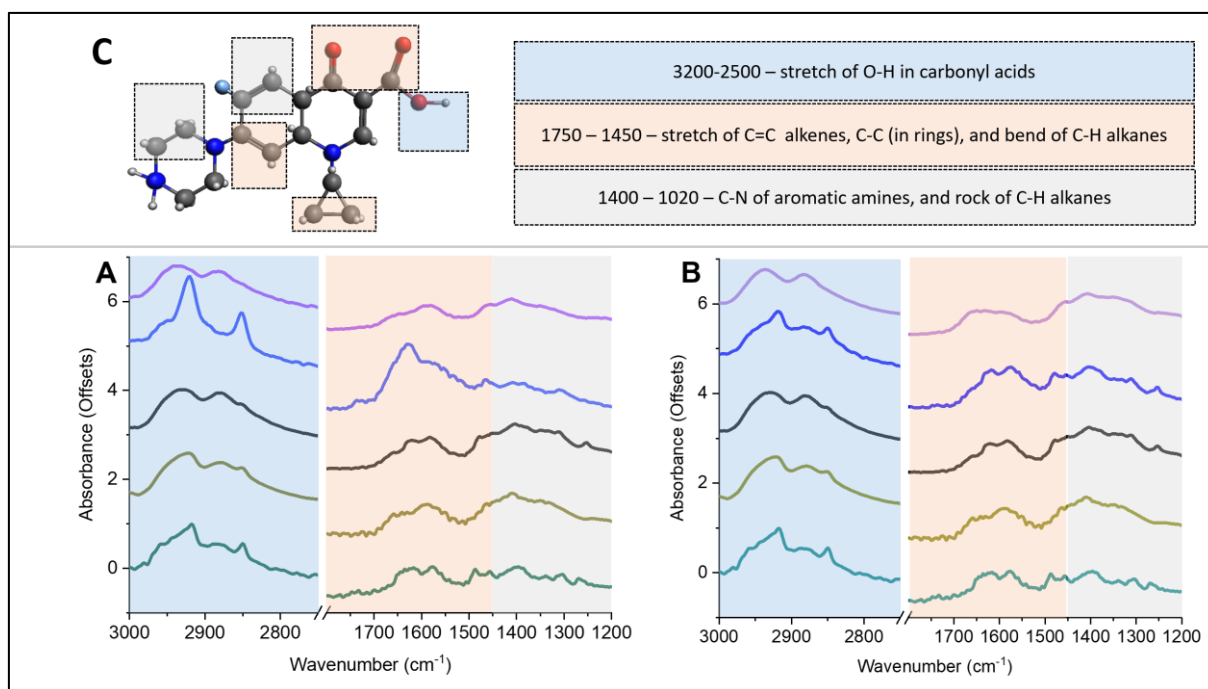
Consistently, only slight spectral changes were observed after 3 h of irradiation, indicating that visible and infrared light cannot promote Cipro degradation (Figure 17A). The irradiation of Cipro for 3 h, with the same solar simulator, in the presence of Co_3O_4 QDs that absorb visible light, resulted in partial bleaching of the compound (Figure 17B). The Cipro photobleaching at 272 nm in the presence of Co_3O_4 QDs could be fitted by exponential decay equation 1 ($R^2 = 0.98945$), which determined a $k_{app} = 0.03 \pm 0.002 \text{ min}^{-1}$. In Equation 1, the C/C_0 offset is the residual absorbance at the decay plateau, A_1 is the decay amplitude, and t_1 is the decay time constant.

$$\frac{C}{C_0} = \frac{C}{C_0} offset + A_1 * e^{(-t/t_1)} \quad (1)$$

As expected, the irradiation of Cipro with UV light resulted in significant photobleaching with $k_{app} = 0.024 \pm 0.001 \text{ min}^{-1}$ calculated by equation 1 with $R^2 = 0.99813$ (Figure 17C). The UV-promoted Cipro photobleaching was considerably enhanced in the presence of Co_3O_4 QDs with a $k_{app} = 0.065 \pm 0.002 \text{ min}^{-1}$ fitted by equation 1 with $R^2 = 0.99821$, respectively (Figure 17D).

Considering that CIPRO photobleaching is promoted by reactions between electronically excited and radical species of fluoroquinolones, its photodegradation was also analyzed by FTIR spectroscopy (Figure 18A, B, and C).

Figure 18. FTIR spectra of CIPRO exposed to UV irradiation under different conditions. A) From bottom to up, FTIR spectra of CIPRO aqueous solution (green line), Co_3O_4 QDs previously corona uncapped by proteinase K (dark yellow line), Co_3O_4 QDs previously corona uncapped by proteinase K plus 2.0 mg/mL of CIPRO before irradiation (black line), pellet of the Co_3O_4 QDs previously corona uncapped by proteinase K and in aqueous solution with CIPRO after 3 h irradiation with a solar simulator (blue line), and supernatant of the same sample described before; B) From bottom to up, FTIR spectra of CIPRO aqueous solution (green line), Co_3O_4 QDs previously corona uncapped by proteinase K (dark yellow line), Co_3O_4 QDs previously corona uncapped by proteinase K plus 2.0 mg/mL of CIPRO before irradiation (black line), pellet of the Co_3O_4 QDs previously corona uncapped by proteinase K and in aqueous solution plus CIPRO, after 60 min of UV-irradiation (blue line), and supernatant of the same sample described before (violet line). In the spectra, the regions corresponding to determine functional groups are highlighted by color panels; C) Molecular structure of CIPRO with the functional groups identified by the regions of FTIR spectra.



Source: Author

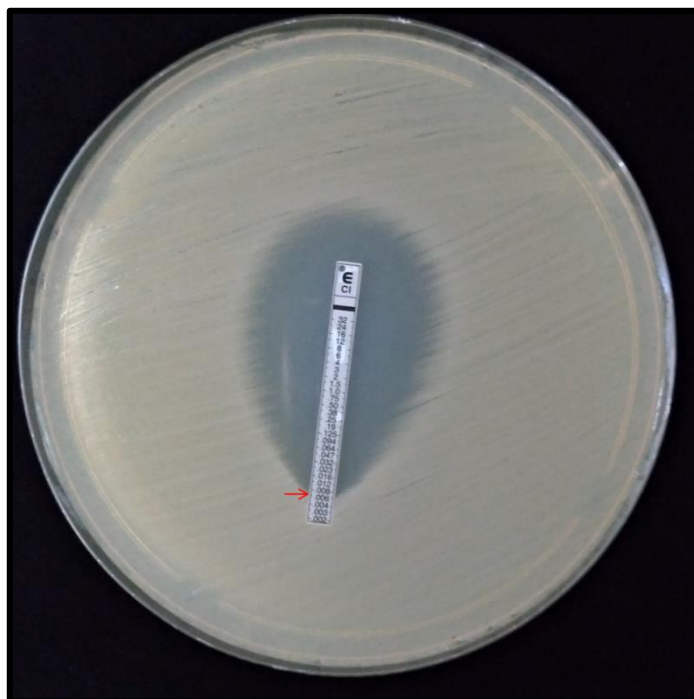
The FTIR spectrum of quinolones presents numerous overlapping bands that make it difficult to ascribe their vibrations unequivocally (ZUPANČIČ et al., 2001). The FTIR spectrum of CIPRO powder is described in the literature as a compound that presents peaks at 3532, 3373, 3089, 2922, 2682, 2620, 1702, 1623, 1492, 1446, 1383, 1342, and 1267 cm^{-1} (BHONGADE; TALATH; DHANESHWAR, 2014; TOFANELLO et al., 2021b) but shifts of these peaks occur in different conditions of the samples. Considering that regions of 3000 and 2800 cm^{-1} have the additional overlapped contribution of water vibrations, the region of 1800–1300 cm^{-1} is the most informative spectral region to detect changes in the structure of

quinolones. In the region of 3000-2800 cm^{-1} , CIPRO aqueous solution presents sharp peaks at 2918 and 2850 cm^{-1} that can be assigned to OH stretching and C-H stretching of $-\text{CH}_2$ groups (HONG et al., 2022; ZUPANČIČ et al., 2001). In Figures 18A and B, green lines, the characteristic band of the carboxylic group vibration in ciprofloxacin hydrochloride hydrate, which is found in the 1700-1720 cm^{-1} region, is absent as expected for the aqueous solution of the antibiotic (TUREL; LEBAN; BUKOVEC, 1997; ZUPANČIČ et al., 2001). Therefore, the overlapped contributions of ($\nu_{\text{as}}(\text{O}-\text{C}-\text{O})$) and symmetric ($\nu_{\text{s}}(\text{O}-\text{C}-\text{O})$) stretching vibrations are observed in the ranges of 1650–1550 cm^{-1} and 1400–1300 cm^{-1} (TUREL; LEBAN; BUKOVEC, 1997; ZUPANČIČ et al., 2001). The FTIR spectrum of Co_3O_4 QDs submitted to corona digestion by proteinase K presents only broad unresolved bands probably resulting from the contribution of amino acids adsorbed on the nanostructure surface (Figure 18A and B, dark yellow lines). In the FTIR spectrum of Co_3O_4 QDs added to CIPRO aqueous solution, the contributions of both components are overlapped, but the band at 1253 cm^{-1} that is assigned to C-O stretching (STAMATAKIS et al., 2010) particularly evidences the presence of CIPRO since it is and absent in the QD spectrum. The aqueous solutions of 2 mg/mL of CIPRO with Co_3O_4 QDs were submitted to irradiation with UV light and the solar simulator for 60 and 180 min, respectively. After irradiation, the samples were submitted to centrifugation for the analysis of pellet and supernatant separately. In Figure 18A and B, the blue lines correspond to the pellets from samples irradiated with UV-light and solar simulator, respectively. The pellet from the sample irradiated with UV light (Figure 18A, blue line) presented a significant increase of the peaks at 2918 and 2850 cm^{-1} that is consistent with formation of additional OH groups resulting from oxidation. These peaks are only slightly increased in the spectrum of pellet from the sample irradiated with solar simulator. The pellet of the sample irradiated with UV-light (Figure 18A, blue line) presented intensification of the peaks at 1629 cm^{-1} that contributes to C=O stretching and 1465 cm^{-1} assigned to C-H bending modes of alkanes (HERRERA-HERRERA et al., 2011). The pellet from the sample submitted to irradiation with the solar simulator did not present significant changes in the region of 1800 – 1200 cm^{-1} . The FTIR spectra of the supernatant obtained from the samples irradiated with UV light and solar simulator are very similar to the spectrum of Co_3O_4 QDs (Figure 18A and B, violet lines). This result suggests that oxidized CIPRO molecules bind to QDs, leading to the formation of aggregates that are pelleted under centrifugation, while Co_3O_4 QDs that are not associated with CIPRO remained in the supernatant. The UV-visible and FTIR obtained for CIPRO exposed to irradiation with Co_3O_4 QDs are consistent with more efficient oxidation of the antibiotic molecule when submitted to the irradiation with UV light. The

supernatant and pellet from the samples irradiated with UV light and solar simulator were tested for bactericidal activity. One crucial issue to be considered in antibiotic degradation is the impairment of the bactericidal action. The elimination of the bactericidal activity avoids the development of bacterial resistance.

The Etest results showed an initial activity of ciprofloxacin against *E.coli* at 0.000006 mg/ml (Figure 19). The concentration of ciprofloxacin used in our experiments was at least 0.0125 mg/ml.

Figure 19. The Etest method. Plate with bacterial growth of *E. coli* and ciprofloxacin strip after 24 hours of incubation. The arrow shows the intersection point between the inhibition halo and the Etest strip at 0.006 µg/ml.

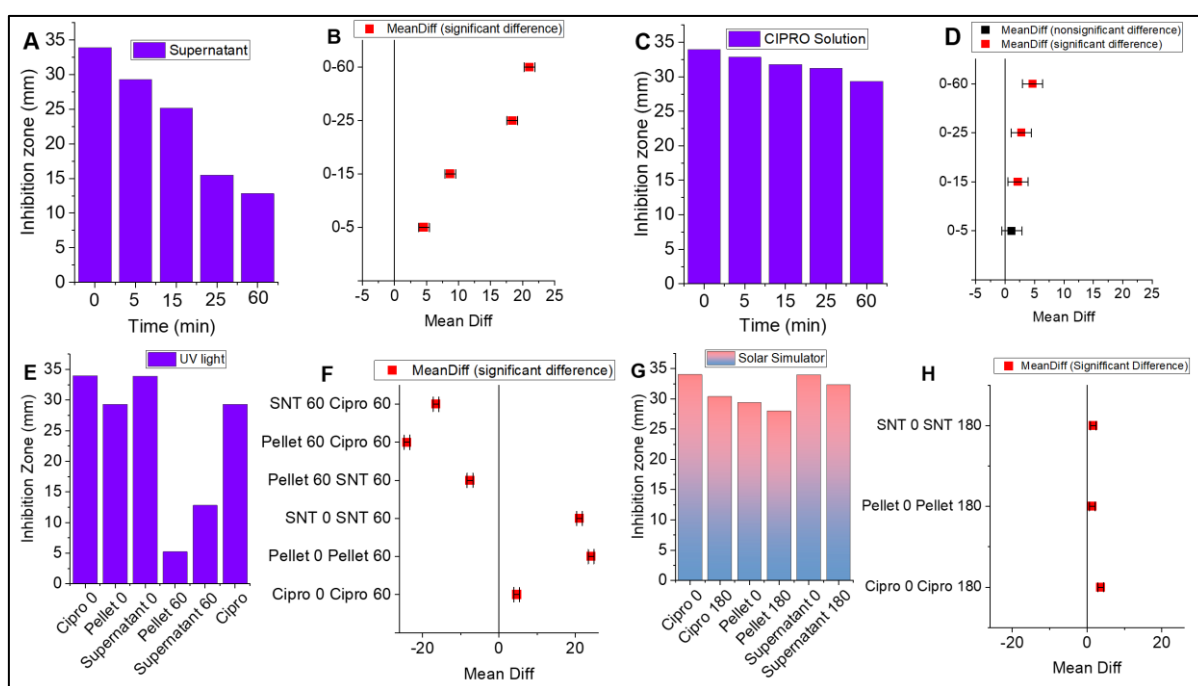


Source: Author

The pellet and supernatant of CIPRO samples had bactericidal activity tested by determining the size of the inhibition zone in triplicate. The results were submitted to Descriptive Statistics and mean comparison by the Bonferroni test using tools available in OriginPro 2021 software (Figure 20A-H). The CIPRO solution (0.025 mg/mL) with Co_3O_4 QDs (0.08 mg/mL) and an aqueous solution of CIPRO (0.025 mg/mL) were both irradiated for 60 min with UV light as described in Material and Methods. During the irradiation with

UV-light and solar simulator, aliquots collected from the samples at different times were centrifugated, and the supernatants and pellets were used to test the capacity of CIPRO to promote inhibition of bacteria growing. Figure 20A shows that the zone of inhibition decreases in a time irradiation-dependent manner. The comparison of the inhibition zones means obtained after 5, 15, 25, and 60 min of irradiation with the result obtained before irradiation (time zero) indicate crescent CIPRO degradation and inactivation (Figure 20B). Even after 5 min of irradiation, a statistically significant inactivation of CIPRO occurred when the irradiation was performed with UV light in the presence of Co_3O_4 QDs (Figure 20B). Figures 20C and D show that only UV-light in the absence of Co_3O_4 QDs is significantly less efficient to promote CIPRO degradation regarding extension of degradation after 60 min of irradiation. Important to note that although FTIR analysis of the supernatant indicated the predominant spectral contribution of Co_3O_4 QDs in the supernatant, CIPRO was present in a concentration enough to promote bacteria destruction since the inhibition zone promoted by supernatant before irradiation had a size approximately equal to that obtained with CIPRO aqueous solution. This result cannot be assigned to the action of Co_3O_4 QDs that were completely unable to inhibit bacteria growth (inhibition zone close to zero). Thus, the decrease of the inhibition zone observed during the irradiation with UV light can only be assigned to the progressive degradation of CIPRO assisted by the ROS produced by Co_3O_4 QDs. The inhibition zone was also determined for the pellet collected from the CIPRO solution containing Co_3O_4 QDs after 60 min of irradiation and compared with the result obtained with the supernatant and UV light alone (Figure 20E and F). Consistently with the FTIR spectrum of the pellet that indicated the presence of CIPRO contribution with spectral changes indicative of degradation by oxidative processes, the smallest inhibition zone was observed for this sample. Considering that Co_3O_4 QDs absorb visible light, a sample of the antibiotic solution in the absence and the presence of the nanostructured material was also submitted to irradiation with a solar simulator that emits only the visible light range (Figures 20G and H). The sample was also fractioned in pellet and supernatant and compared with CIPRO aqueous solution irradiated with a solar simulator. In these conditions, a minimal decrease of inhibition zones with values statistically different from the controls was obtained only after 180 minutes of irradiation.

Figure 20. Effect of irradiation and Co_3O_4 QDs on CIPRO degradation. A) Time of UV-irradiation-dependent inactivation of CIPRO present in supernatant evaluated by the decrease of inhibition zone. The mean values were obtained from three independent experiments; B) Comparison of the mean values presented in A, by Bonferroni analysis; C) Time of UV-irradiation-dependent inactivation of CIPRO solution evaluated by the decrease of inhibition zone. The mean values were obtained from three independent experiments; D) Comparison of the mean values presented in C, by Bonferroni analysis; Time of UV-irradiation-dependent inactivation of CIPRO present in supernatant evaluated by the decrease of inhibition zone. The mean values were obtained from three independent experiments; E) Comparative analysis of the degree of CIPRO inactivation after 60 min in the absence and presence of Co_3O_4 QDs. The sample containing nanostructured material was fractionated by centrifugation before adding on agar plates; F) Bonferroni comparative analysis of the results presented in E showing that pellet and supernatant were more efficient than CIPRO irradiated with UV-light, and the pellet was more efficient than supernatant.



Source: Author

4.4. Conclusion

Tomato seed extract can be efficiently used in a green and sustainable method to produce cobalt oxide quantum dots with photocatalytic activity, which was previously demonstrated to be able to inactivate coronaviruses. In the present work, photocatalytic activity was used to inactivate the antibiotic CIPRO, which is considered an emerging pollutant in fresh and saltwater sources. Co_3O_4 QDs promoted significant photodegradation of CIPRO in the presence of UV light, which alone showed little efficiency for the inactivation of the antibiotic. In the presence of the QDs, CIPRO oxidized by UV forms aggregates with

the nanostructures that sediment by centrifugation and constituted the fraction of the sample with a more significant loss of activity against bacterial growth. Considering that QDs absorb visible light, the low efficiency of this irradiation to promote photodegradation may be due to two factors, the binding of the antibiotic to the surface of the quantum dots, reducing the absorption of light, and synergistic action between quinolone excited states resulting from UV absorption and the catalytic action of the QD due to the presence of oxygen vacancies in its crystalline structure. Considering that the solar spectrum has UV and visible light, Co_3O_4 QDs are promising for the photodegradation of CIPRO in water sources exposed to natural sunlight.

5. CONCLUSION

Quantum dots of Co_3O_4 were fabricated using cobalt II nitrate hexahydrate with tomato (*Solanum Lycopersicum* L.) seed extract, at room temperature. The QDs were characterized by UV-visible spectrophotometry, high-resolution transmission electron microscopy (HRTEM), X-ray excited photoelectron spectrometer (XPS), Fourier transform infrared spectrometer (FTIR), and superconducting quantum interference device (SQUID). Co_3O_4 QDs present chirality evidenced by magnetic circular dichroism. Consistent with previous Mössbauer data, electron paramagnetic resonance (EPR) revealed the presence of iron ferritin as the dominant iron ion signal in tomato seeds. The use of the pulp was able to produce cobalt oxide NPs. Commercially purified horse spleen ferritin was equally efficient to produce Co_3O_4 QDs. The use of red grape tomato seeds resulted in Co_3O_4 nanoparticles with low crystallinity. Co_3O_4 QDs were incorporated in a cotton textile that acquired virucidal activity.

REFERENCES

- ABDULRAZAQ, Y. et al. Classification, Potential Routes and Risk of Emerging Pollutants/Contaminant. In: **Emerging Contaminants**. [s.l.] IntechOpen, 2021.
- ALIVISATOS, A. P. Semiconductor clusters, nanocrystals, and quantum dots. **Science**, v. 271, n. 5251, p. 933–937, 16 fev. 1996.
- AMBE, S. Mössbauer study of iron in the tomato plant. **International Journal of Radiation Applications and Instrumentation. Part**, v. 40, n. 8, p. 671–675, jan. 1989.
- AMETA, R. et al. Photocatalysis. In: **Advanced Oxidation Processes for Wastewater Treatment: Emerging Green Chemical Technology**. [s.l.] Elsevier Inc., 2018. p. 135–175.
- ANANDABABU, K. et al. Single-step benzene hydroxylation by cobalt(ii) catalysts: Via a cobalt(iii)-hydroperoxo intermediate. **Catalysis Science and Technology**, v. 10, n. 8, p. 2540–2548, abr. 2020.
- ANH TRAN, V. et al. Solar-light-driven photocatalytic degradation of methyl orange dye over Co₃O₄-ZnO nanoparticles. **Materials Letters**, v. 284, p. 128902, fev. 2021.
- ATARASSI, M. E. et al. Avaliação de classificadora de cilindros divergentes para tomate “Carmen”. **Engenharia Agrícola**, v. 30, n. 2, p. 334–345, abr. 2010.
- AWAD, Y. M. et al. Veterinary antibiotics contamination in water, sediment, and soil near a swine manure composting facility. **Environmental Earth Sciences** **2013 71:3**, v. 71, n. 3, p. 1433–1440, 19 maio 2013.
- BAI, H.; LIU, Z.; SUN, D. D. Hierarchical ZnO/Cu “corn-like” materials with high photodegradation and antibacterial capability under visible light. **Physical chemistry chemical physics : PCCP**, v. 13, n. 13, p. 6205–6210, 7 abr. 2011.
- BALEJČÍKOVÁ, L. et al. The effect of solution pH on the structural stability of magnetoferritin. **Colloids and Surfaces B: Biointerfaces**, v. 156, p. 375–381, ago. 2017.
- BANI-YASEEN, A. D. et al. On the photophysicochemical properties of selected fluoroquinolones: Solvatochromic and fluorescence spectroscopy study. **Journal of Fluorescence**, v. 23, n. 1, p. 93–101, jan. 2013.
- BEEGAM, A. et al. Environmental Fate of Zinc Oxide Nanoparticles: Risks and Benefits. In: **Toxicology - New Aspects to This Scientific Conundrum**. [s.l.] InTech, 2016.
- BELLOTTTO, O. et al. Peptide gelators to template inorganic nanoparticle formation. **Gels**, v. 7, n. 1, p. 1–14, 2021.
- BENKOULA, S. et al. Water adsorption on TiO₂ surfaces probed by soft X-ray spectroscopies: Bulk materials vs. isolated nanoparticles. **Scientific Reports**, v. 5, n. 1, p. 1–11, out. 2015.
- BERA, D. et al. Quantum dots and their multimodal applications: A review. **Materials**, v. 3, n. 4, p. 2260–2345, 2010.
- BESSEGATO, G. G. et al. Achievements and Trends in Photoelectrocatalysis: from Environmental to Energy Applications. **Electrocatalysis**, v. 6, n. 5, p. 415–441, set. 2015.

BHONGADE, B.; TALATH, S.; DHANESHWAR, S. A Validated Method for the Quantitation of Ciprofloxacin Hydrochloride Using Diffuse Reflectance Infrared Fourier Transform Spectroscopy. **International Journal of Spectroscopy**, v. 2014, p. 1–6, fev. 2014.

BORASE, H. P. et al. **Plant extract: A promising biomatrix for ecofriendly, controlled synthesis of silver nanoparticles***Applied Biochemistry and Biotechnology* Humana Press Inc., , 2014. Disponível em: <<https://pubmed.ncbi.nlm.nih.gov/24622849/>>. Acesso em: 14 jan. 2021

BRITO, A. M. M. et al. Proteins and peptides at the interfaces of nanostructures. **Anais da Academia Brasileira de Ciencias**, v. 91, n. 4, p. 1–17, 2019.

BRONZATO, J. D. et al. Virucidal, photocatalytic and chiromagnetic cobalt oxide quantum dots. **Applied Surface Science**, v. 576, n. PA, p. 151847, 2022.

BROQVIST, P. A DFT Study on CO Oxidation over Co₃O₄. **Journal of Catalysis**, v. 210, n. 1, p. 198–206, ago. 2002.

BURDA, C. et al. **Chemistry and properties of nanocrystals of different shapes***Chemical Reviews* American Chemical Society , , abr. 2005. Disponível em: <<https://pubs.acs.org/doi/abs/10.1021/cr030063a>>. Acesso em: 12 jan. 2021

CAÇO, A. I. et al. Solubility of Antibiotics in Different Solvents. Part II. Non-Hydrochloride Forms of Tetracycline and Ciprofloxacin. **Industrial & Engineering Chemistry Research**, v. 47, n. 21, p. 8083–8089, nov. 2008.

CAI, Z. et al. Hierarchical Cu@Co-decorated CuO@Co₃O₄ nanostructure on Cu foam as efficient self-supported catalyst for hydrogen evolution reaction. **Journal of Alloys and Compounds**, v. 882, p. 160749, nov. 2021.

CANTARELLI, P. R.; REGITANO-D'ARCE, M. A. B.; PALMA, E. R. Physicochemical characteristics and fatty acid composition of tomato seed oils from processing wastes. **Scientia Agricola**, v. 50, n. 1, p. 117–120, maio 1993.

CERCENADO, E. et al. Evaluation of direct E-test on lower respiratory tract samples: a rapid and accurate procedure for antimicrobial susceptibility testing. **Diagnostic microbiology and infectious disease**, v. 58, n. 2, p. 211–216, jun. 2007.

CHAN, S. H. S. et al. **Recent developments of metal oxide semiconductors as photocatalysts in advanced oxidation processes (AOPs) for treatment of dye wastewater***Journal of Chemical Technology and Biotechnology* John Wiley & Sons, Ltd, , 1 set. 2011. Disponível em: <<https://onlinelibrary.wiley.com/doi/full/10.1002/jctb.2636>>. Acesso em: 8 jan. 2021

CHIANCONE, E. et al. **Iron and proteins for iron storage and detoxification***BioMetals*. [s.l: s.n.].

CLEUVERS, M. Initial risk assessment for three β -blockers found in the aquatic environment. **Chemosphere**, v. 59, n. 2, p. 199–205, abr. 2005.

CUQUERELLA, M. C. et al. Triplet excimers of fluoroquinolones in aqueous media. **Journal of Physical Chemistry A**, v. 116, n. 21, p. 5030–5038, maio 2012.

DAOUD, S. et al. Fast and direct analysis of oxidation levels of oil-in-water emulsions using

ATR-FTIR. **Food Chemistry**, v. 293, p. 307–314, set. 2019.

DEORI, K. et al. Morphology Controlled Synthesis of Nanoporous Co₃O₄ Nanostructures and Their Charge Storage Characteristics in Supercapacitors. **ACS Applied Materials & Interfaces**, v. 5, n. 21, p. 10665–10672, out. 2013.

DEWI, N. O. M.; YULIZAR, Y.; BAGUS APRIANDANU, D. O. Green synthesis of Co₃O₄ nanoparticles using Euphorbia heterophylla L. leaves extract: characterization and photocatalytic activity. **IOP Conference Series: Materials Science and Engineering**, v. 509, n. 1, p. 012105, 1 abr. 2019.

DIALLO, A. et al. Green synthesis of Co₃O₄ nanoparticles via Aspalathus linearis: Physical properties. <http://mc.manuscriptcentral.com/tgcl>, v. 8, n. 3–4, p. 30–36, 2 out. 2015.

DIALLO, A. et al. Magnetic behavior of biosynthesized Co₃O₄ nanoparticles. **Journal of Magnetism and Magnetic Materials**, v. 424, p. 251–255, fev. 2017.

DIAS, C. F. B.; NANTES, I. L.; RODRIGUES, F. A. Photoreduction of cytochrome c by UV-irradiated TiO₂ particles. **Abstracts of Papers of the American Chemical Society**, 2004.

DJURIŠIĆ, A. B.; LEUNG, Y. H.; CHING NG, A. M. **Strategies for improving the efficiency of semiconductor metal oxide photocatalysis** *Materials Horizons* Royal Society of Chemistry, , 1 jul. 2014. Disponível em: <<http://xlink.rsc.org/?DOI=c4mh00031e>>. Acesso em: 8 jan. 2021

DONG, S. et al. **Recent developments in heterogeneous photocatalytic water treatment using visible light-responsive photocatalysts: A review** *RSC Advances*, 2015.

DUBEY, S. et al. Facile and green synthesis of highly dispersed cobalt oxide (Co₃O₄) nano powder: Characterization and screening of its eco-toxicity. **Advanced Powder Technology**, v. 29, n. 11, p. 2583–2590, 1 nov. 2018.

DUYNE, V. 2003 Nature Enantiospecific electrodeposition of a chiral catalyst.pdf. v. 425, n. October, p. 6–9, 2003.

EDVINSSON, T. Optical quantum confinement and photocatalytic properties in two-, one- and zero-dimensional nanostructures. **Royal Society Open Science**, v. 5, n. 9, set. 2018.

EUCAST Definitive Document E.DEF 3.1, June 2000: Determination of minimum inhibitory concentrations (MICs) of antibacterial agents by agar dilution. **Clinical microbiology and infection : the official publication of the European Society of Clinical Microbiology and Infectious Diseases**, v. 6, n. 9, p. 509–515, 2000.

FARHADI, S.; JAVANMARD, M.; NADRI, G. Characterization of Cobalt Oxide Nanoparticles Prepared by the Thermal Decomposition. **Acta Chimica Slovenica**, p. 335–343, 2016.

FERRER, I.; ZWEIGENBAUM, J. A.; THURMAN, E. M. Analysis of 70 Environmental Protection Agency priority pharmaceuticals in water by EPA Method 1694. **Journal of Chromatography A**, v. 1217, n. 36, p. 5674–5686, set. 2010.

FINLAYSON-PITTS, B. J.; SWEETMAN, L. L.; WEISSBART, B. A Fourier transform infrared spectrometry study of the reactions of phosphatidylcholines with gaseous N₂O₅ and

NO2. **Toxicology and Applied Pharmacology**, v. 89, n. 3, p. 438–448, jul. 1987.

FRADE, V. M. F. et al. **Environmental contamination by fluoroquinolones** **Brazilian Journal of Pharmaceutical Sciences**, 2014.

GÁLVEZ, N. et al. Apoferritin-encapsulated Ni and Co superparamagnetic nanoparticles. **Journal of Materials Chemistry**, v. 16, n. 26, p. 2757–2761, 2006.

GÁLVEZ, N. et al. Apoferritin as a nanoreactor for preparing metallic nanoparticles. **Comptes Rendus Chimie**, v. 11, n. 10, p. 1207–1212, out. 2008a.

GÁLVEZ, N. et al. Apoferritin as a nanoreactor for preparing metallic nanoparticles. **Comptes Rendus Chimie**, v. 11, n. 10, p. 1207–1212, 1 out. 2008b.

GANHARUL, G. K. Q. et al. Disclosing the hidden presence of Ti^{3+} ions in different TiO_2 crystal structures synthesized at low temperature and photocatalytic evaluation by methylene blue photobleaching. **Journal of Materials Research**, v. 36, n. 16, p. 3353–3365, ago. 2021.

GENG, B. et al. A facile coordination compound precursor route to controlled synthesis of Co_3O_4 nanostructures and their room-temperature gas sensing properties. **Journal of Materials Chemistry**, v. 18, n. 41, p. 4977–4984, 2008.

GHOSH, S. et al. Increasing the Efficiency of Water Splitting through Spin Polarization Using Cobalt Oxide Thin Film Catalysts. **Journal of Physical Chemistry C**, v. 124, n. 41, p. 22610–22618, out. 2020.

GOMES, B. P. F. DE A. et al. In vitro antimicrobial activity of calcium hydroxide pastes and their vehicles against selected microorganisms. **Brazilian dental journal**, v. 13, n. 3, p. 155–161, 2002.

GUO, H. G. et al. Photochemical degradation of ciprofloxacin in UV and UV/ H_2O_2 process: Kinetics, parameters, and products. **Environmental Science and Pollution Research**, v. 20, n. 5, p. 3202–3213, maio 2013a.

GUO, W. et al. Degradation of antibiotics amoxicillin by Co_3O_4 -catalyzed peroxymonosulfate system. **Environmental Progress & Sustainable Energy**, v. 32, n. 2, p. 193–197, 1 jul. 2013b.

HAN, L.; YANG, D. P.; LIU, A. Leaf-templated synthesis of 3D hierarchical porous cobalt oxide nanostructure as direct electrochemical biosensing interface with enhanced electrocatalysis. **Biosensors and Bioelectronics**, v. 63, p. 145–152, 15 jan. 2015.

HARIHARAN, C. Photocatalytic degradation of organic contaminants in water by ZnO nanoparticles: Revisited. **Applied Catalysis A: General**, v. 304, n. 1–2, p. 55–61, 10 maio 2006.

HERRERA-HERRERA, A. V. et al. Oxidized multi-walled carbon nanotubes for the dispersive solid-phase extraction of quinolone antibiotics from water samples using capillary electrophoresis and large volume sample stacking with polarity switching. **Journal of Chromatography A**, v. 1218, n. 31, p. 5352–5361, ago. 2011.

HIKONO, T. et al. Novel method for making nanodot arrays using a cage-like protein. **Japanese Journal of Applied Physics, Part 2: Letters**, v. 42, n. 4 A, p. 398–400, 2003.

HISATOMI, T.; KUBOTA, J.; DOMEN, K. **Recent advances in semiconductors for photocatalytic and photoelectrochemical water splitting** *Chemical Society Reviews* Royal Society of Chemistry, , 21 nov. 2014.

HONG, J. et al. Ionic liquid-based dispersive liquid–liquid microextraction followed by magnetic solid-phase extraction for determination of quinolones. *Microchimica Acta*, v. 189, n. 1, p. 1–10, dez. 2022.

HOSEIN, H. A. et al. Iron and cobalt oxide and metallic nanoparticles prepared from ferritin. *Langmuir*, v. 20, n. 23, p. 10283–10287, 2004.

HOSSEINI-KOUPAEI, M. et al. Catalytic activity, structure and stability of proteinase K in the presence of biosynthesized CuO nanoparticles. *International Journal of Biological Macromolecules*, v. 122, p. 732–744, 1 fev. 2019.

HU, L. et al. Surface active sites on Co₃O₄ nanobelt and nanocube model catalysts for CO oxidation. *Nano Research*, v. 3, n. 5, p. 363–368, maio 2010.

HUANG, P. et al. Dye-Loaded Ferritin Nanocages for Multimodal Imaging and Photothermal Therapy. *Advanced Materials*, v. 26, n. 37, p. 6401–6408, 1 out. 2014.

HUANG, Y.; MOSLEH, I.; ABBASPOURRAD, A. Impact of protein/peptide templates on metallic nanoparticle synthesis and applications. *Nano-Structures & Nano-Objects*, v. 30, p. 100864, 1 abr. 2022.

INGENBOSCH, K. N. et al. Singlet-Oxygen Generation by Peroxidases and Peroxygenases for Chemoenzymatic Synthesis. *ChemBioChem*, v. 22, n. 2, p. 398–407, jan. 2021.

IRAVANI, S. et al. **Synthesis of silver nanoparticles: Chemical, physical and biological methods** *Research in Pharmaceutical Sciences* Isfahan University of Medical Sciences(IUMS), , 1 dez. 2014. Disponível em: </pmc/articles/PMC4326978/?report=abstract>. Acesso em: 14 jan. 2021

JIANG, B. et al. Biom mineralization Synthesis of the Cobalt Nanozyme in SP94-Ferritin Nanocages for Prognostic Diagnosis of Hepatocellular Carcinoma. *ACS applied materials & interfaces*, v. 11, n. 10, p. 9747–9755, mar. 2019.

JIMÉNEZ-TOTOTZINTLE, M. et al. Removal of contaminants of emerging concern (CECs) and antibiotic resistant bacteria in urban wastewater using UVA/TiO₂/H₂O₂ photocatalysis. *Chemosphere*, v. 210, p. 449–457, 1 nov. 2018.

JOUYANDEH, M. et al. **Quantum dots for photocatalysis: synthesis and environmental applications** *Green Chemistry* The Royal Society of Chemistry, , jul. 2021.

KAPUGE, T. K. et al. Photo-generated reactive oxygen species assisted tandem amine homocoupling and amine-alcohol cross-coupling reaction on mesoporous spinel cobalt oxide. *Applied Catalysis B: Environmental*, v. 268, p. 118386, jul. 2020.

KARTHIKEYAN, K. G.; MEYER, M. T. Occurrence of antibiotics in wastewater treatment facilities in Wisconsin, USA. *Science of The Total Environment*, v. 361, n. 1–3, p. 196–207, 15 maio 2006.

KASYUTICH, O. et al. Silver Ion Incorporation and Nanoparticle Formation inside the Cavity of Pyrococcus furiosus Ferritin: Structural and Size-Distribution Analyses. *Journal of*

the American Chemical Society, v. 132, n. 10, p. 3621–3627, 2010.

KHAN, I.; SAEED, K.; KHAN, I. Nanoparticles: Properties, applications and toxicities. **Arabian Journal of Chemistry**, v. 12, n. 7, p. 908–931, 1 nov. 2019.

KHAN, M. M.; ADIL, S. F.; AL-MAYOUF, A. Metal oxides as photocatalysts. **Journal of Saudi Chemical Society**, v. 19, n. 5, p. 462–464, 2015.

KIM, T.-K. et al. Degradation of ciprofloxacin and inactivation of ciprofloxacin resistant *E. faecium* during UV-LED (275 nm)/chlorine process. **Chemical Engineering Journal**, v. 394, p. 124803, ago. 2020.

KLEM, M. T.; YOUNG, M.; DOUGLAS, T. Biomimetic magnetic nanoparticles. **Materials Today**, v. 8, n. 9, p. 28–37, set. 2005.

KOMBAIAH, K. et al. Green Synthesis of Co_3O_4 Nanorods for Highly Efficient Catalytic, Photocatalytic, and Antibacterial Activities. **Journal of Nanoscience and Nanotechnology**, v. 19, n. 5, p. 2590–2598, 2 dez. 2018.

KOMBAIAH, K. et al. Green Synthesis of Co_3O_4 Nanorods for Highly Efficient Catalytic, Photocatalytic, and Antibacterial Activities. **Journal of Nanoscience and Nanotechnology**, v. 19, n. 5, p. 2590–2598, maio 2019.

KUNDU, S. et al. Formation of shape-selective magnetic cobalt oxide nanowires: Environmental application in catalysis studies. **CrystEngComm**, v. 15, n. 3, p. 482–497, 2013.

LI, J. et al. Nanoparticle Superlattices as Efficient Bifunctional Electrocatalysts for Water Splitting. **Journal of the American Chemical Society**, 2015.

LI, W. et al. Highly efficient activation of peroxydisulfate by cobalt sulfide hollow nanospheres for fast ciprofloxacin degradation. **Journal of Hazardous Materials**, v. 389, maio 2020.

LIAO, X. et al. Biodegradation of antibiotic ciprofloxacin: pathways, influential factors, and bacterial community structure. **Environmental Science and Pollution Research**, 2016.

LIENAU, K. et al. Microwave-Hydrothermal Tuning of Spinel-Type Co_3O_4 Water Oxidation Catalysts. **Frontiers in Chemistry**, v. 8, p. 473, jun. 2020.

LIU, H.; WANG, C.; WANG, G. **Photocatalytic Advanced Oxidation Processes for Water Treatment: Recent Advances and Perspective** Chemistry - An Asian Journal John Wiley and Sons Ltd, , out. 2020.

LIU, T. C.; PELL, W. G.; CONWAY, B. E. Stages in the development of thick cobalt oxide films exhibiting reversible redox behavior and pseudocapacitance. **Electrochimica Acta**, v. 44, n. 17, p. 2829–2842, 1999.

LIU, Y. et al. Carbon-based quantum dots (QDs) modified ms/tz-BiVO_4 heterojunction with enhanced photocatalytic performance for water purification. **Journal of Alloys and Compounds**, v. 881, p. 160437, nov. 2021.

LORENZO, F.; NAVARATNAM, S.; ALLEN, N. S. Formation of secondary triplet species after excitation of fluoroquinolones in the presence of relatively strong bases. **Journal of the**

American Chemical Society, v. 130, n. 37, p. 12238–12239, set. 2008.

MA, C. Y. et al. Mesoporous Co_3O_4 and $\text{Au/Co}_3\text{O}_4$ Catalysts for Low-Temperature Oxidation of Trace Ethylene. **Journal of the American Chemical Society**, v. 132, n. 8, p. 2608–2613, mar. 2010.

MAEKAWA, S. **Concepts in Spin Electronics**. United States: Oxford Publisher Press, 2006.

MAKHLOUF, S. A. et al. Structural, electrical and optical properties of Co_3O_4 nanoparticles. **Superlattices and Microstructures**, v. 64, p. 107–117, dez. 2013.

MAKOFANE, A.; MOTAUNG, D. E.; HINTSHO-MBITA, N. C. Photocatalytic degradation of methylene blue and sulfisoxazole from water using biosynthesized zinc ferrite nanoparticles. **Ceramics International**, v. 47, n. 16, p. 22615–22626, 15 ago. 2021.

MALWAL, D.; PACKIRISAMY, G. Recent Advances in the Synthesis of Metal Oxide (MO) Nanostructures. In: **Synthesis of Inorganic Nanomaterials**. [s.l.] Elsevier, 2018. p. 255–281.

MELNÍKOVÁ, L. et al. Effect of iron oxide loading on magnetoferritin structure in solution as revealed by SAXS and SANS. **Colloids and Surfaces B: Biointerfaces**, v. 123, p. 82–88, nov. 2014.

MENEZES, L. R. et al. Photo-induced Electron Transfer from Hematite and Zinc Oxide Nanostructures to Cytochrome C: Systems Applicable to Spintronics. p. 1–9, 2019.

MENEZES, L. R. et al. Nanostructured Hematite Decorated with Gold Nanoparticles for Functionalization and Biocompatibility. **Physica Status Solidi (A) Applications and Materials Science**, v. 217, n. 5, p. 1–10, 2020.

MENG, F. et al. Bioengineered Tunable Memristor Based on Protein Nanocage. **Small**, v. 10, n. 2, p. 277–283, jan. 2014.

MUTHUMARIAPPAN, S. Synthesis and characterization of ciprofloxacin–zinc (II) complex and assay studies in pharmaceutical drugs. **Journal of Pharmacy Research**, v. 6, n. 4, p. 437–441, abr. 2013.

NASSAR, M. Y.; AHMED, I. S. Hydrothermal synthesis of cobalt carbonates using different counter ions : An efficient precursor to nano-sized cobalt oxide (Co_3O_4). v. 30, p. 2431–2437, 2011.

NAUERT, S. L. et al. Cyclohexane oxidative dehydrogenation over copper oxide catalysts. **Journal of Catalysis**, v. 341, p. 180–190, set. 2016.

NAVEEN, A. N.; SELLADURAI, S. Tailoring structural , optical and magnetic properties of spinel type cobalt oxide (Co_3O_4) by manganese doping. v. 457, p. 251–262, 2015.

NETSKINA, O. V. et al. Aqueous-alkaline NaBH_4 solutions: The influence of hydride decomposition on catalytic properties of Co_3O_4 . **Catalysis Communications**, v. 85, p. 9–12, out. 2016.

NGUYEN, H.; EL-SAFTY, S. A. Meso- and macroporous Co_3O_4 nanorods for effective VOC gas sensors. **Journal of Physical Chemistry C**, v. 115, n. 17, p. 8466–8474, 2011.

NOSAKA, Y.; NOSAKA, A. **Understanding Hydroxyl Radical ($\bullet\text{OH}$) Generation Processes in Photocatalysis**ACS Energy LettersAmerican Chemical Society, , jul. 2016.

NOZIK, A. J. et al. Semiconductor quantum dots and quantum dot arrays and applications of multiple exciton generation to third-generation photovoltaic solar cells. **Chemical Reviews**, v. 110, n. 11, p. 6873–6890, 10 nov. 2010.

PAES DE BARROS, M. et al. Oxidative/Nitrative Mechanism of Molsidomine Mitotoxicity Assayed by the Cytochrome c Reaction with SIN-1 in Models of Biological Membranes. **Chemical Research in Toxicology**, v. 33, n. 11, p. 2775–2784, nov. 2020.

PAGAR, T. et al. A Review on Bio-Synthesized Co₃O₄ Nanoparticles Using Plant Extracts and their Diverse Applications. **Journal of Chemical Reviews**, v. 1, n. 4, p. 260–270, 1 out. 2019a.

PAGAR, T. et al. A review on bio-synthesized Co₃O₄ nanoparticles using plant extracts and their diverse applications. **Journal of Chemical Reviews**, v. 1, n. 4, p. 260–270, 10 out. 2019b.

PARVEKAR, P. et al. The minimum inhibitory concentration (MIC) and minimum bactericidal concentration (MBC) of silver nanoparticles against *Staphylococcus aureus*. **Biomaterial investigations in dentistry**, v. 7, n. 1, p. 105–109, 1 jan. 2020.

PHAN, M. H. et al. Exchange bias effects in iron oxide-based nanoparticle systems. **Nanomaterials**, v. 6, n. 11, 2016.

POHLE, W. et al. **FTIR-spectroscopic characterization of phosphocholine-headgroup model compounds**. Journal of Molecular Structure. **Anais...Elsevier**, maio 2001

RAO, V. N. et al. **Sustainable hydrogen production for the greener environment by quantum dots-based efficient photocatalysts: A review** **Journal of Environmental Management** Academic Press, , out. 2019.

RODRIGUEZ-MOZAZ, S. et al. Occurrence of antibiotics and antibiotic resistance genes in hospital and urban wastewaters and their impact on the receiving river. **Water Research**, v. 69, p. 234–242, 1 fev. 2015.

SANTOS, H. F. et al. Charge separation of photosensitized phenothiazines for applications in catalysis and nanotechnology. **Dyes and Pigments**, v. 177, p. 108314, jun. 2020.

SARATALE, R. G. et al. New insights on the green synthesis of metallic nanoparticles using plant and waste biomaterials: current knowledge, their agricultural and environmental applications. **Environmental Science and Pollution Research**, v. 25, n. 11, p. 10164–10183, 2018.

SHARMA, P. C. et al. Ciprofloxacin: review on developments in synthetic, analytical, and medicinal aspects. **Journal of Enzyme Inhibition and Medicinal Chemistry**, v. 25, n. 4, p. 577–589, ago. 2010.

SHI, W. et al. Fabrication of ternary Ag₃PO₄/Co₃(PO₄)₂/g-C₃N₄ heterostructure with following Type II and Z-Scheme dual pathways for enhanced visible-light photocatalytic activity. **Journal of Hazardous Materials**, v. 389, p. 121907, maio 2020.

SIVACHIDAMBARAM, M. et al. A novel synthesis protocol for Co₃O₄ nanocatalysts and their catalytic applications. **RSC Advances**, v. 7, n. 62, p. 38861–38870, 8 ago. 2017.

SRINIVASAN, V.; WEIDNER, J. W. Capacitance studies of cobalt oxide films formed via

electrochemical precipitation. **Journal of Power Sources**, v. 108, n. 1–2, p. 15–20, 2002.

STAMATAKIS, G. et al. Analysis and aging of unsaturated polyester resins in contemporary art installations by NMR spectroscopy. **Analytical and Bioanalytical Chemistry**, v. 398, n. 7–8, p. 3203–3214, dez. 2010.

TAKADA, S. et al. Intraparticle Magnetic Properties of Co₃O₄ Nanocrystals. **Nano Letters**, v. 1, n. 7, p. 379–382, jul. 2001.

TANG, C. W.; WANG, C. BIN; CHIEN, S. H. Characterization of cobalt oxides studied by FT-IR, Raman, TPR and TG-MS. **Thermochimica Acta**, v. 473, n. 1–2, p. 68–73, 2008.

TATON, T. A. Nanoscale Materials in Chemistry Edited by Kenneth J. Klabunde (Kansas State University). Wiley-Interscience: New York. 2001. xi + 292 pp. \$99.95. ISBN: 0-471-38395-3. **Journal of the American Chemical Society**, v. 124, n. 35, p. 10629–10630, set. 2002.

TIAN, K. et al. Nanostructure modulation of Co₃O₄ films by varying anion sources for pseudocapacitor applications. **Solid State Ionics**, v. 371, p. 115756, nov. 2021.

TOFANELLO, A. et al. Conversion of ferritin ferrihydrite core to magnetite by gold ions binding and the derived nanoparticle formation. **Journal of Nanostructure in Chemistry** **2021**, p. 1–16, 15 jul. 2021a.

TOFANELLO, A. et al. Photodegradation of Ciprofloxacin-Zinc Complexes Produced at the Interface of ZnO and Cu-Doped ZnO Crystals. **Materials Research**, v. 24, n. 6, p. 20210198, 27 ago. 2021b.

TOLBERT, S. H. et al. Comparison of quantum confinement effects on the electronic absorption spectra of direct and indirect gap semiconductor nanocrystals. **Physical Review Letters**, v. 73, n. 24, p. 3266–3269, 12 dez. 1994.

TOLEDO, G. G. DE et al. Promising Nanostructured Materials against Enveloped Virus. **Anais da Academia Brasileira de Ciências**, v. 92, n. 4, 2020.

TORRES, S.; PALACIO, R.; LÓPEZ, D. Support effect in Co₃O₄-based catalysts for selective partial oxidation of glycerol to lactic acid. **Applied Catalysis A: General**, v. 621, p. 118199, jul. 2021.

TUREL, I.; LEBAN, I.; BUKOVEC, N. Crystal structure and characterization of the bismuth(III) compound with quinolone family member (ciprofloxacin). Antibacterial study. **Journal of Inorganic Biochemistry**, v. 66, n. 4, p. 241–245, jun. 1997.

TYO, E. C. et al. Oxidative dehydrogenation of cyclohexane on cobalt oxide (Co₃O₄) nanoparticles: The effect of particle size on activity and selectivity. **ACS Catalysis**, 2012.

UCHIDA, M. et al. The ferritin superfamily: Supramolecular templates for materials synthesis. **Biochimica et Biophysica Acta (BBA) - General Subjects**, v. 1800, n. 8, p. 834–845, ago. 2010a.

UCHIDA, M. et al. The ferritin superfamily: Supramolecular templates for materials synthesis. **Biochimica et Biophysica Acta (BBA) - General Subjects**, v. 1800, n. 8, p. 834–845, 1 ago. 2010b.

UCHIDA, M. et al. The Ferritin Superfamily: Supramolecular Templates for Materials Synthesis. **Bone**, v. 23, n. 1, p. 1–7, 2014.

VAYSSIÈRES, L. et al. Purpose-built anisotropic metal oxide material: 3D highly oriented microrod array of ZnO. **Journal of Physical Chemistry B**, v. 105, n. 17, p. 3350–3352, 3 maio 2001.

VOON, C. H. et al. Synthesis and preparation of metal oxide powders. In: **Metal Oxide Powder Technologies**. [s.l.] Elsevier, 2020. p. 31–65.

WANG, J. et al. Fabrication of a ternary heterostructure BiVO₄ quantum dots/C60/g-C3N₄ photocatalyst with enhanced photocatalytic activity. **Journal of Physics and Chemistry of Solids**, v. 136, p. 109164, jan. 2020a.

WANG, J. et al. Earth-abundant transition-metal-based bifunctional catalysts for overall electrochemical water splitting: A review. **Journal of Alloys and Compounds**, v. 819, p. 153346, abr. 2020b.

WANG, Q.; WANG, P.; YANG, Q. Occurrence and diversity of antibiotic resistance in untreated hospital wastewater. **Science of the Total Environment**, v. 621, p. 990–999, abr. 2018.

WANG, Y.; HERRON, N. **Nanometer-sized semiconductor clusters: Materials synthesis, quantum size effects, and photophysical properties** *Journal of Physical Chemistry*, jan. 1991. Disponível em: <<https://pubs.acs.org/doi/abs/10.1021/j100155a009>>. Acesso em: 12 jan. 2021

WANG, Z. et al. Biomineralization-Inspired Synthesis of Copper Sulfide-Ferritin Nanocages as Cancer Theranostics. **ACS Nano**, v. 10, n. 3, p. 3453–3460, 2016a.

WANG, Z. et al. Biomineralization-Inspired Synthesis of Copper Sulfide–Ferritin Nanocages as Cancer Theranostics. **ACS Nano**, v. 10, n. 3, p. 3453–3460, mar. 2016b.

WANG, Z. et al. Biomineralization-Inspired Synthesis of Copper Sulfide-Ferritin Nanocages as Cancer Theranostics. **ACS Nano**, v. 10, n. 3, p. 3453–3460, 22 mar. 2016c.

WEN, C. et al. Self-healing catalysts: Co₃O₄ nanorods for Fischer–Tropsch synthesis. **Chem. Commun.**, v. 50, n. 35, p. 4575–4578, 2014.

WU, W. et al. Degradation of organic compounds by peracetic acid activated with Co₃O₄: A novel advanced oxidation process and organic radical contribution. **Chemical Engineering Journal**, v. 394, p. 124938, ago. 2020.

XU, H. et al. Preparation and performance of Co₃O₄-NiO composite electrode material for supercapacitors. **RSC Advances**, v. 4, n. 30, p. 15511–15517, 2014.

XUE, J. et al. Surfactant-free large scale synthesis of Co₃O₄ quantum dots at room temperature. **Advanced Powder Technology**, v. 27, n. 5, p. 2019–2024, 2016.

XUE, L.; DENG, D.; SUN, J. Magnetoferritin: Process, Prospects, and Their Biomedical Applications. **International Journal of Molecular Sciences**, v. 20, n. 10, p. 2426, maio 2019.

YADAV, S. et al. Synthesis and characterization of nickel oxide/cobalt oxide nanocomposite

for effective degradation of methylene blue and their comparative electrochemical study as electrode material for supercapacitor application. **International Journal of Hydrogen Energy**, v. In Press, fev. 2022.

YANG, S. et al. Oxygen-Vacancy Abundant Ultrafine Co_3O_4 /Graphene Composites for High-Rate Supercapacitor Electrodes. **Advanced Science**, v. 5, n. 4, p. 1700659, abr. 2018.

YANG, S. et al. Enhanced photocatalytic activity of g-C₃N₄ quantum dots/Bi_{3.64}Mo_{0.36}O_{6.55} nanospheres composites. **Journal of Solid State Chemistry**, v. 287, p. 121347, jul. 2020.

YANG, X. et al. Recent advances in photodegradation of antibiotic residues in water. **Chemical Engineering Journal**, v. 405, p. 126806, 1 fev. 2021.

YEOM, J. et al. Chiro-magnetic nanoparticles and gels. **Science**, v. 359, n. 6373, p. 309–314, 2018.

YOFFE, A. D. Semiconductor quantum dots and related systems: Electronic, optical, luminescence and related properties of low dimensional systems. **Advances in Physics**, v. 50, n. 1, p. 1–208, 1 jan. 2001.

YU, X. et al. Photocatalytic degradation of ciprofloxacin using Zn-doped Cu₂O particles: Analysis of degradation pathways and intermediates. **Chemical Engineering Journal**, v. 374, p. 316–327, out. 2019.

ZHANG, N. et al. Oxide Defect Engineering Enables to Couple Solar Energy into Oxygen Activation. **Journal of the American Chemical Society**, v. 138, n. 28, p. 8928–8935, jul. 2016.

ZHANG, Q. Q. et al. Comprehensive evaluation of antibiotics emission and fate in the river basins of China: Source analysis, multimedia modeling, and linkage to bacterial resistance. **Environmental Science and Technology**, v. 49, n. 11, p. 6772–6782, jun. 2015.

ZHANG, S. et al. The Size Flexibility of Ferritin Nanocage Opens a New Way to Prepare Nanomaterials. **Small**, v. 13, n. 37, p. 1701045, out. 2017.

ZHANG, W. et al. Enhanced Electrochemical Water Splitting with Chiral Molecule-Coated Fe₃O₄ Nanoparticles. **ACS Energy Letters**, v. 3, n. 10, p. 2308–2313, out. 2018.

ZHAO, X. et al. Synergetic effect of carbon sphere derived from yeast with magnetism and cobalt oxide nanochains towards improving photodegradation activity for various pollutants. **Applied Catalysis B: Environmental**, v. 220, p. 137–147, 1 jan. 2018.

ZHENG, Y. et al. Ultrathin mesoporous Co₃O₄ nanosheets with excellent photo-/thermo-catalytic activity. **Journal of Materials Chemistry A**, v. 4, n. 1, p. 105–112, 15 dez. 2015.

ZHENG, Y. et al. Chirality Effects in Peptide Assembly Structures. **Frontiers in Bioengineering and Biotechnology**, v. 9, 22 jun. 2021.

ZHOU, P.; YU, J.; JARONIEC, M. **All-solid-state Z-scheme photocatalytic systems** *Advanced Materials* Wiley-VCH Verlag, , 6 ago. 2014. Disponível em: <<http://doi.wiley.com/10.1002/adma.201400288>>. Acesso em: 8 jan. 2021

ZUPANČIČ, M. et al. Synthesis and characterization of two novel zinc(II) complexes with

ciprofloxacin. Crystal structure of $[\text{C}_{17}\text{H}_{19}\text{N}_3\text{O}_3\text{F}]_2 \cdot [\text{ZnCl}_4] \cdot 2\text{H}_2\text{O}$. **Croatica Chemica Acta**, v. 74, n. 1, p. 61–74, 2001.

APPENDIX A - Previous research

CONVERSION OF FERRITIN FERRIHYDRITE CORE TO MAGNETITE BY GOLD IONS BINDING AND THE DERIVED NANOPARTICLE FORMATION.

(Summarized article)

Authors: Aryane Tofanello, Julia D. Bronzato, Carlos Rettori, Otaciro R. Nascimento & Iseli L. Nantes-Cardoso

Periodic: Journal of Nanostructures in Chemistry 12, 401–416 (2022).

Publication Date: Received 27 December 2020. Accepted 08 July 2021. Published 15 July 2021.

The study was initiated with the first motivation to develop a method for AuNP synthesis using vegetable extracts under conditions in which their protein contents could be preserved. A diversity of fruit extracts, including tomato extract, was able to produce AuNPs under mild conditions. However, only the synthesis with tomato extract was also produced, and unexpectedly, magnetic nanoparticles. Therefore, we propose to thoroughly investigate the use of natural ion-storage protein as a platform for the combined synthesis of both nanostructures, specifying the specific role of the biomolecule during the process.

Tomato extract was used to synthesize AuNPs at room temperature with high stirring in an attempt to establish a variation in the AuNP synthesis method that could preserve native biomolecules to confer biocompatibility with low-cost production. The unexpected formation of magnetic material, characterized as Fe_3O_4 , and concomitant with AuNP formation, led us to investigate the iron source, the mechanism of magnetite formation, and the role played by gold salt in the synthesis. Ferritin ferrihydrite core was used as the iron source for the biomineralization of magnetite.

Ferritin nanocage structures have been used to encapsulate guest molecules and promote metallic crystal growth based on their capacity for pH-induced disassembly and reassembly. For these materials produced using ferritin nanocage, several technological applications have been described (MENG et al., 2014; ZHANG et al., 2017). The proposal that endogenous ferritin is the iron source for Fe_3O_4 synthesis facilitated by gold ions raised the question of why the synthesis of gold nanoparticles with other plant extracts in mild conditions did not simultaneously produce Fe_3O_4 , considering that ferritin is ubiquitous in

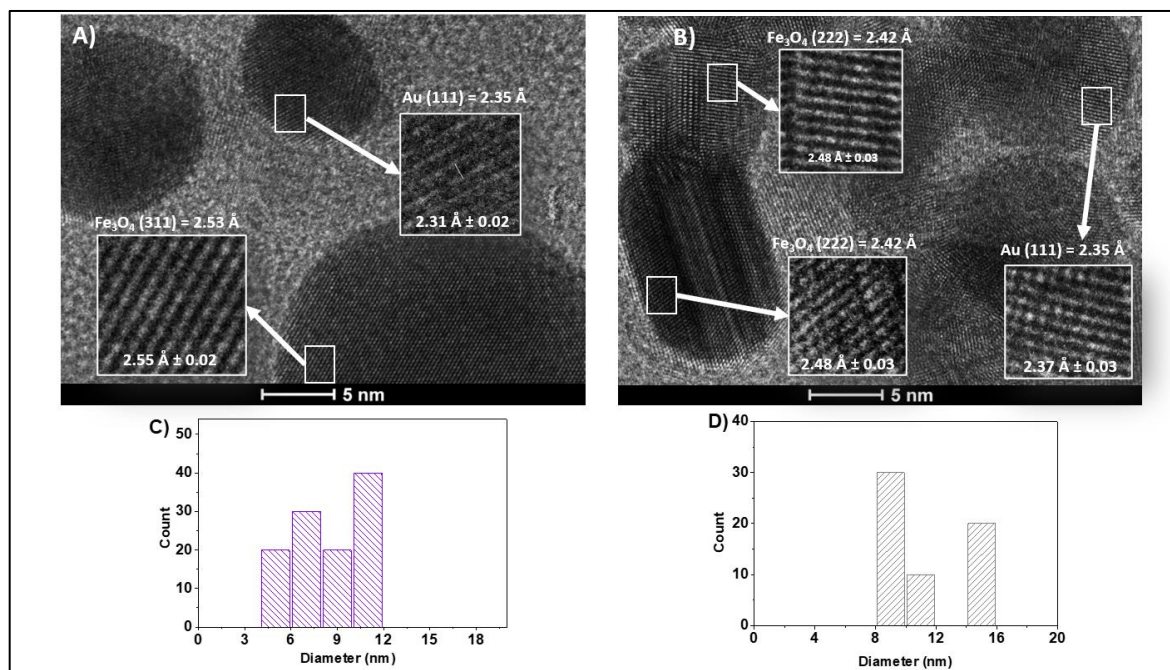
almost all living organisms. The answer comes from previous Mössbauer studies on the iron content of a diversity of plants. That study revealed that only tomato seems to accumulate almost all of its iron content in a ferritin-like species (PHAN et al., 2016). The Mössbauer parameters determined for tomato ferric ions in seeds, stems, and leaves are far from those determined for iron-sulfur, heme proteins, and iron-citrate common in plants (AMBE, 1989). The isomer shift and quadrupole splitting of tomato leaves, stems, and roots are closest to ferritin, the iron storage protein broadly present in plants and animals.

To elucidate whether the formation of magnetic material in tomato extract was promoted exclusively by gold salts, we repeated the synthesis method with AgNO_3 . Similarly, silver nanoparticles concomitant with magnetic material were also obtained under identical synthesis conditions, only replacing HAuCl_4 with AgNO_3 solution at a concentration of 10 mM. The time expended for the appearance of the silver nanoparticle SPR band was similar to that observed for AuNPs. However, the use of silver salt delayed the formation of the magnetic material and decreased its yield. The synthesis using gold salts was repeated five times, and the yield of AuNPs and magnetic materials varied according to the tomato ripening step and source.

To elucidate whether the endogenous iron content in tomatoes was effective in producing Fe_3O_4 , iron salts were added to the reaction medium using tomato sources in which the yield of magnetic material was relatively low. Under these conditions, the addition of iron salt to tomato extract did not increase the yield of magnetic nanoparticles, indicating a specific endogenous source of iron in tomatoes.

To investigate the direct imaging of the crystallographic structure at the atomic level, the AuNPs, and the magnetic material were characterized by HRTEM, which corroborated Fe_3O_4 and AuNP phase formations (Figures 21A and B). The images reveal that there was no formation of nanohybrid nanoparticles, alloys, or heterojunctions. Representative HRTEM images of the as-synthesized AuNPs and Fe_3O_4 with lattice fringe spacing and the corresponding histograms of magnetite and gold nanoparticles are shown in Figures 21A, B, C, and D, respectively.

Figure 171. The HRTEM of the Au and Fe₃O₄ nanoparticles produced with tomato extract and HAuCl₄ solution submitted to stirring are shown in A) and B). The boxed regions have been enlarged to analyze the lattice spacing, which was consistent with metallic nanoparticles and magnetite. The corresponding histograms of Au and Fe₃O₄ nanoparticles are shown in C) and D).



Source: Aryane Tofanello

The determination of the interplanar spacing identified both Au and Fe₃O₄ NPs. For the gold nanoparticles, the interplanar spacing of 2.3 Å is consistent with the (111) facet of the typical *fcc* phase of metallic gold (JCPDS no. 04-0784). In magnetic nanoparticles, the identified lattice fringes correspond well to the (311) plane with an interplanar distance of 2.5 Å, which is characteristic of the *fcc* phase of magnetite (JCPDS no. 19-0629). The series of the histograms of AuNPs (Figure 21C) and Fe₃O₄ (Figure 21D) show that the AuNPs and Fe₃O₄ NPs have mean diameters of 8.6 ± 2.1 nm and 11 ± 2.5 nm, respectively, compatible with the diameter of the ferritin hollow nanocages with a gain of polydispersity and relaxed quaternary structure resulting from exposure to extreme pH values (BALEJČÍKOVÁ et al., 2017; MELNÍKOVÁ et al., 2014). Therefore, we conceived the formation of the first metal nuclei of magnetite inside the ferritin nanocage, as reported in previous studies (KLEM; YOUNG; DOUGLAS, 2005; XUE; DENG; SUN, 2019).

Tomato extract was reported as containing almost all its iron content in ferritin and here we demonstrated that the ferritin iron core can be converted to nanoparticulated Fe₃O₄ concomitantly with AuNP formation when challenged by gold ions. Considering the similar

results obtained with mammalian ferritin, it is reasonable to presume that the iron storage protein is the biomolecule responsible for the simultaneous synthesis of metallic nanoparticles and Fe_3O_4 in an environmentally benign and scalable approach. The results presented encouraged us to investigate other metallic salts, such as cobalt. In the case of cobalt, the magnetite was not formed, a change between the iron ions and the cobalt happened; the iron dissipated in the solution, and after washing the solution, the iron was removed.

APPENDIX B - Future perspectives

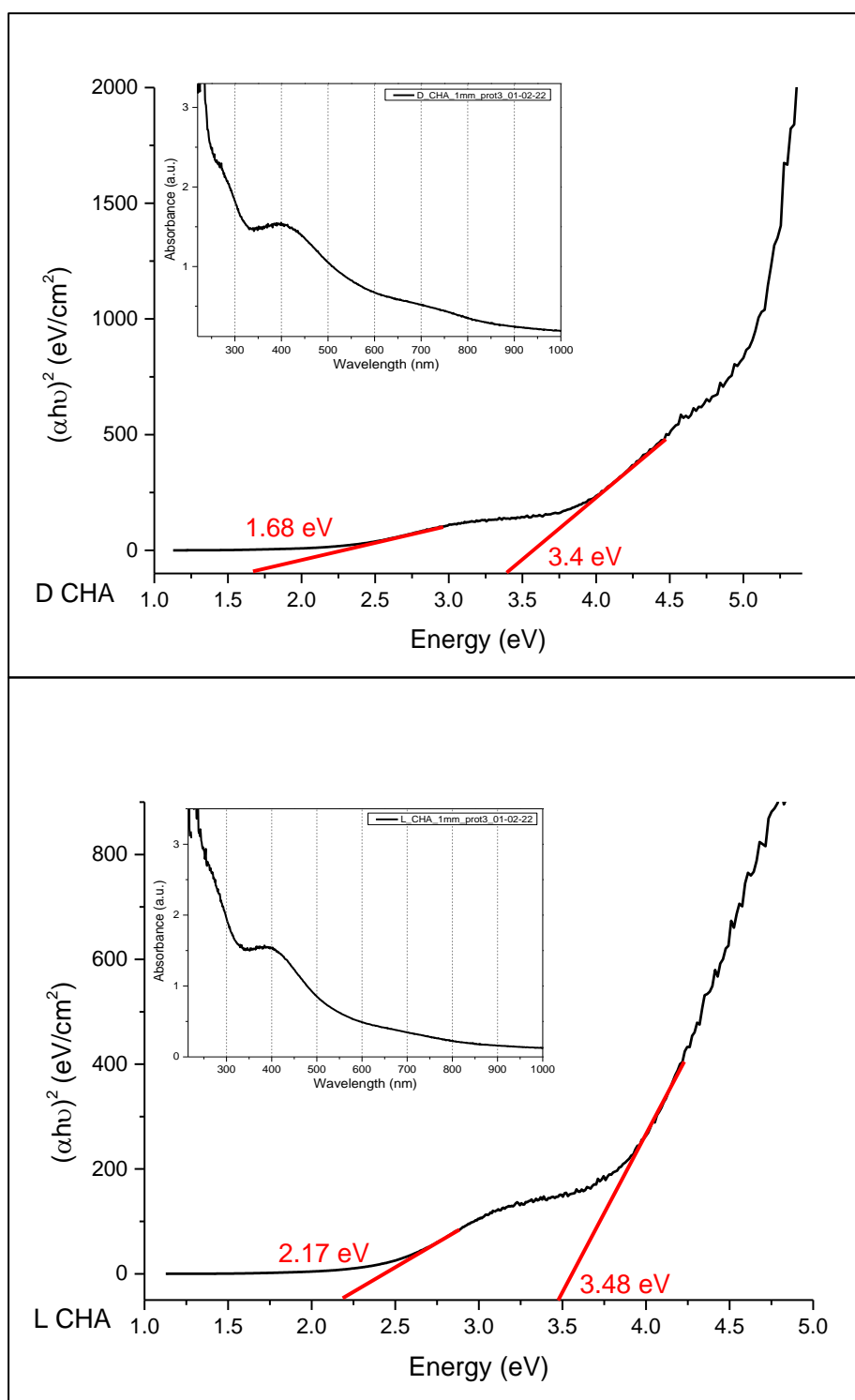
Chirality is a very active field of study; it is present in chemistry, medicine, and biology and has potential applications in chiral sensing, catalysis, and optical devices (HUANG; MOSLEH; ABBASPOURRAD, 2022). Peptides and proteins are considered chiral molecules (ZHENG et al., 2021), and are used as spin filters (BRITO et al., 2019). The use of peptides as biotemplates is well known, they bind into the metal nuclei and create a reducing environment, which promotes the reduction of metallic ions to nanoparticles (BELLOTTO et al., 2021).

Cobalt oxide nanoparticles were produced using the peptide “CHA” as a template. The peptide is formed by the amino acids cysteine, histidine, and alanine. Chiral peptides D-CHA and L-CHA were used, and this study aims to produce chiral cobalt oxide nanoparticles.

The peptide “CHA” was previously produced with the amino acids cysteine, histidine, and alanine. The stock concentration produced was 1mg/mL in water, with 40uL of acetic acid. 600uL of the stock was mixed in an Eppendorf, at room temperature, with 100uL of 200mM cobalt nitrate hexahydrate, 800 uL of 100mM sodium citrate, and 200uL of 1M HCl, until reached pH 2, then 200uL of 100mM NaOH, until reach pH 13. After the mixture, the sample had a bluish and later brownish color. After one week, the sample was dark-brown color, and the UV-Visible spectroscopy showed bands compatible with the formation of cobalt oxide nanoparticles.

The UV-visible spectra (figure 22) were used to determine the direct bandgap energies by the Tauc plot (insets). The insets show the plots of $(\alpha h\nu)^2$ vs. photo energy (eV) based on the respective UV–visible spectra. The values of bandgap energy are intersected with the photon energy ($h\nu$) axis from the extrapolation of the optical absorption coefficient to zero.

Figure 182. UV-Visible spectra and the corresponding Tauc plots of the nanoparticles synthesized with D CHA (top image) and L CHA (bottom image).



Source: Author

The bandgap energies obtained for the cobalt oxide nanoparticles synthesized using D CHA are 1.68 and 3.4 eV whereas the synthesis carried out with L CHA are 2.17 and 3.48 eV. These values result in bandgap energy differences ($\Delta E = E_{g1} - E_{g2}$) of 1.72 and 1.31 eV, respectively.

Figures 23 and 24 show the FEG (Field Emission Gun – Scanning Electron Microscope) images and NTA (nanoparticle tracking analysis) from the NPs produced with D CHA and L CHA respectively. FEG shows a mean diameter of 20nm, meanwhile NTA shows a mean diameter of 100nm. However, the aggregation process of the NPs difficult for the acquirer of the images at FEG and NTA.

Figure 23. Cobalt oxide nanoparticles synthesized with D CHA peptide. FEG images and NTA confirmed the formation and the size, respectively.

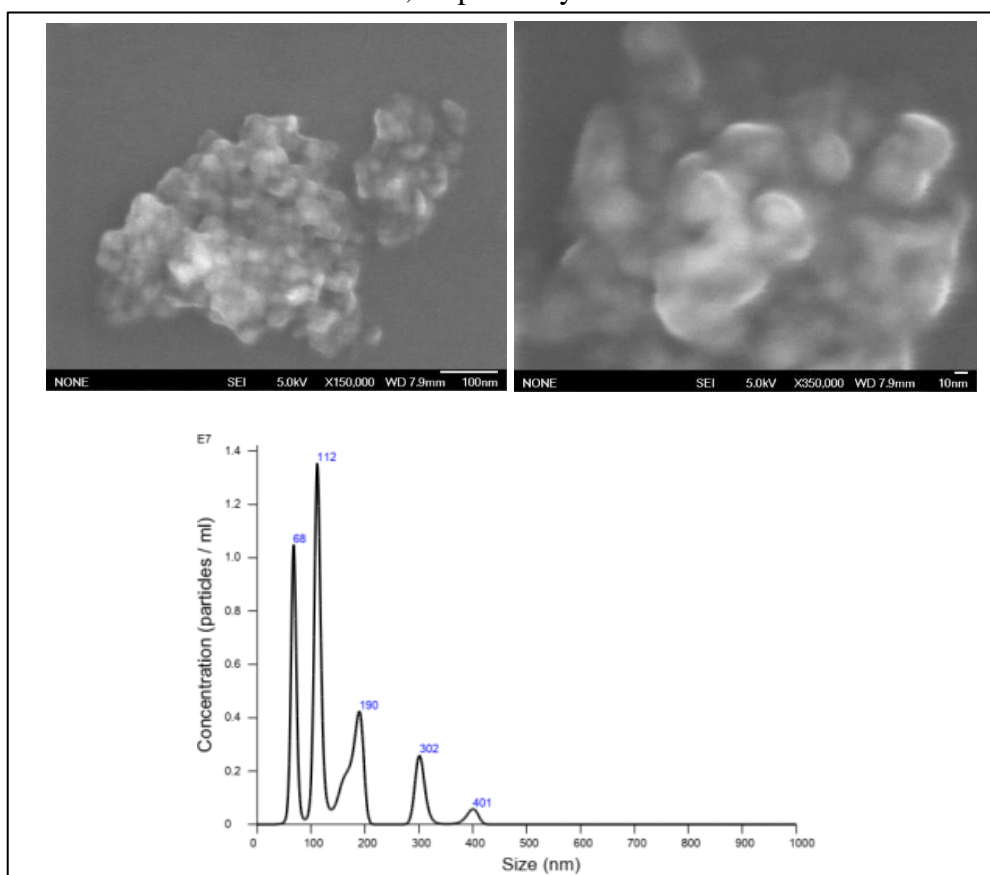
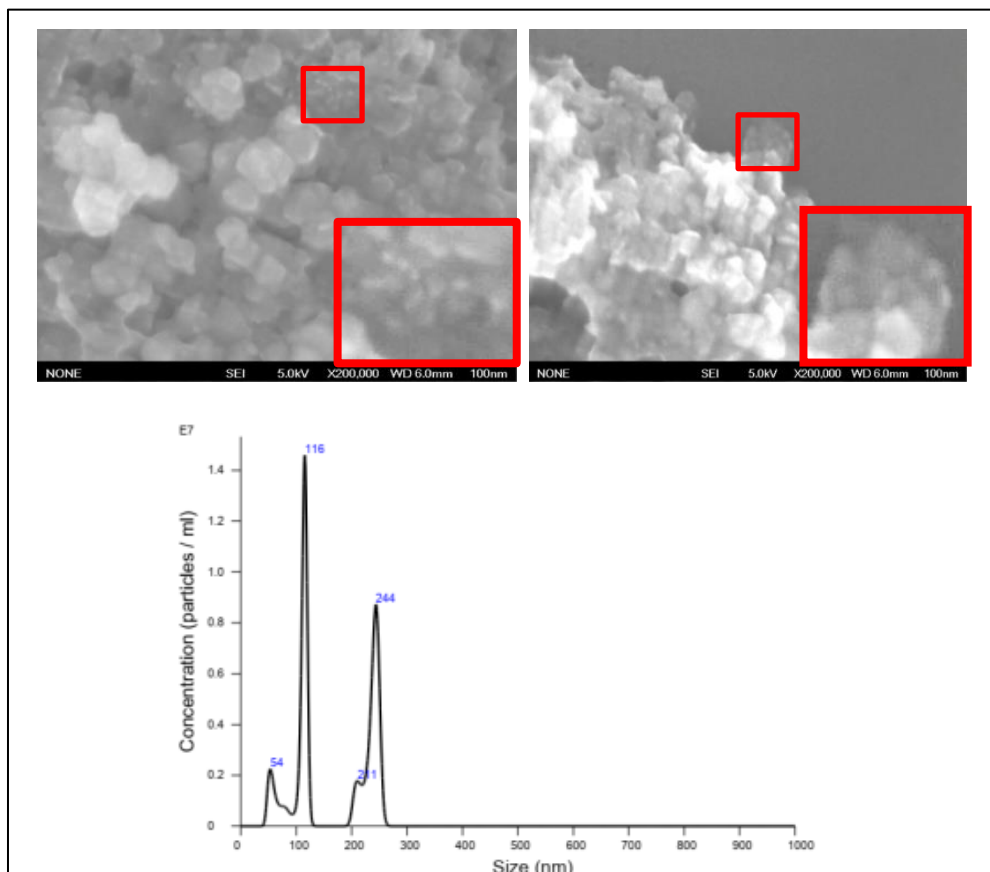


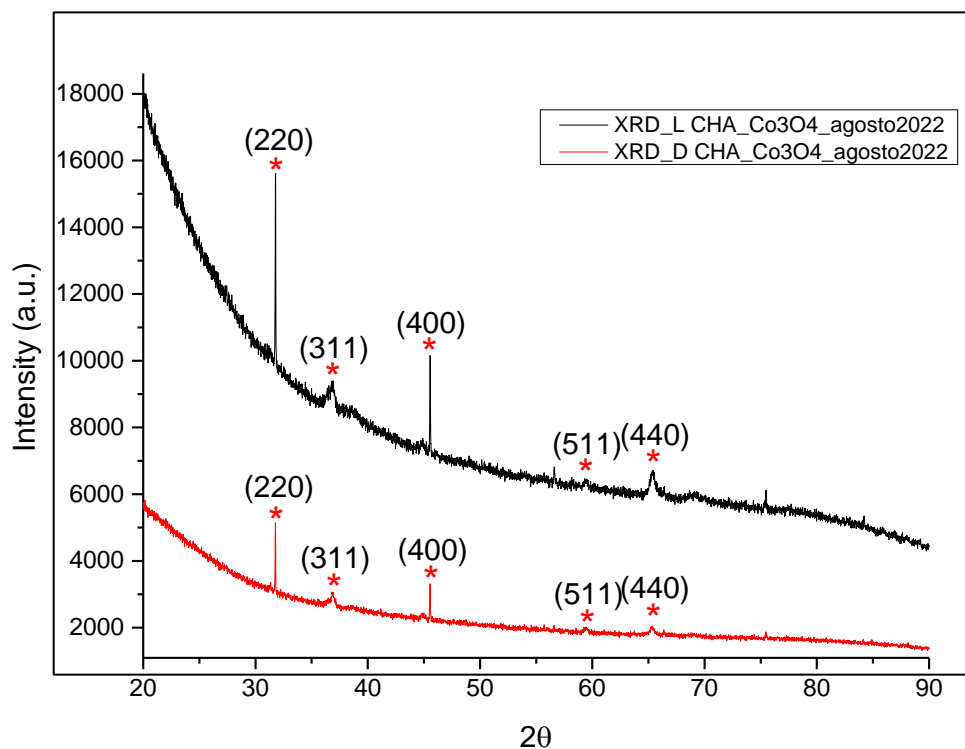
Figure 194. Cobalt oxide nanoparticles synthesized with L CHA peptide. FEG images and NTA confirmed the formation and the size, respectively.



Source: Author

Figure 25 shows the X-ray diffraction spectra, L CHA (black line) and D CHA (red line). A thin film was prepared at the sample holder, until dry. The peaks obtained at 36.9° , 45.5° , 59.5° , and 65.3° are indexed to (311), (400), (511) and (440) respectively, and can be assigned to the planes of cobalt oxide.

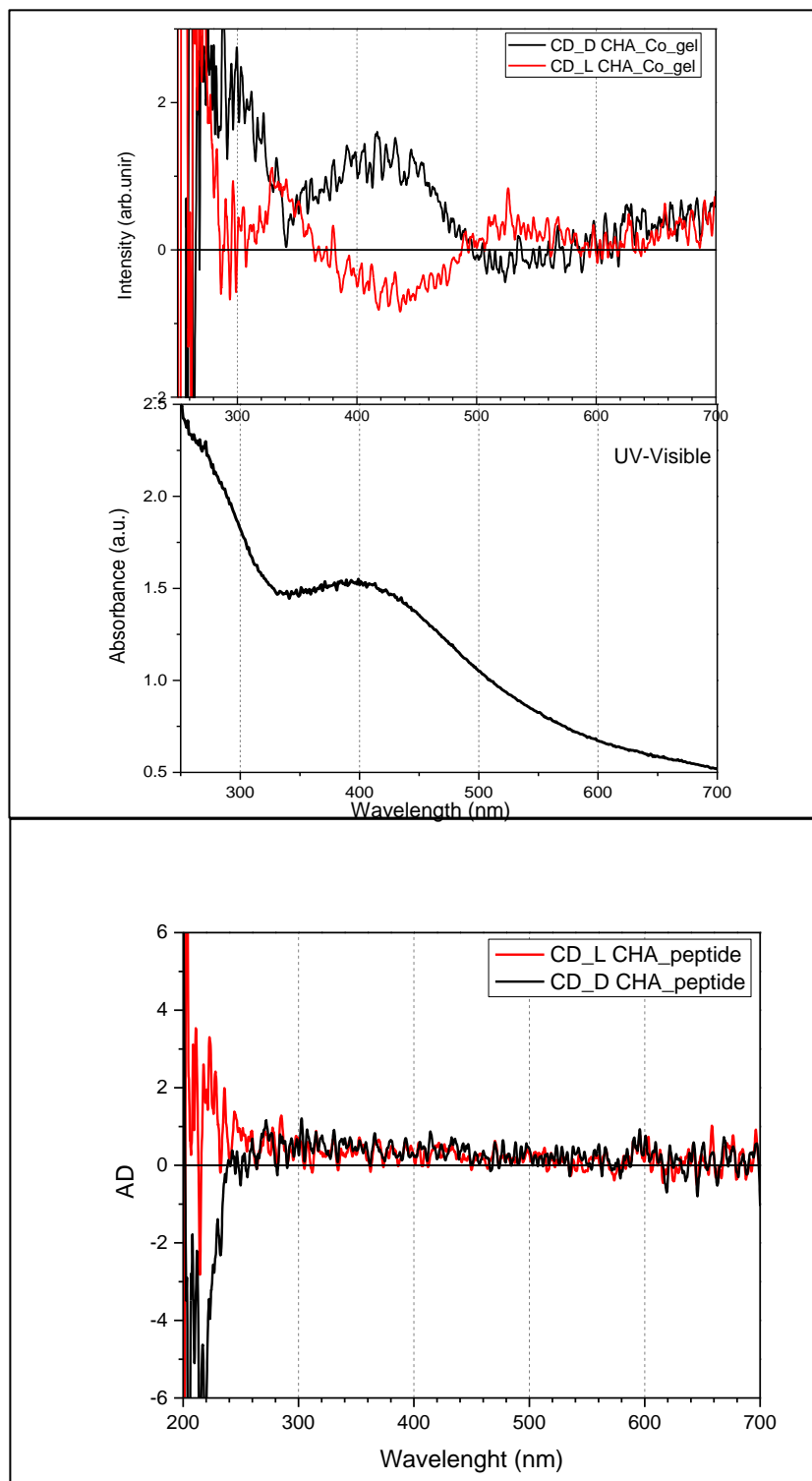
Figure 205. X-ray diffraction spectra (XRD) with copper radiation of the NPs synthesized with L CHA (black line) and D CHA (red line).



Source: Author.

Considering that crystal growth possibly occurred in association with chiral molecules, the presence of circular dichroism (CD) signals, originating from chiral molecules adsorbed on the material surface and distortion of the crystal structure was investigated by CD techniques, in figure 26.

Figure 216. Up images: Circular dichroism (CD) spectra of the immobilized material in a gel, synthesized with D CHA (black line) and L CHA (red line), and UV-Visible spectra of the nanoparticles, to compare that the CD has a signal at the same region of the UV-Vis. Bottom image: CD spectra of the peptide by itself, D CHA (black line) and L CHA (red line).



Source: Author.

Circular dichroism spectroscopy was used to investigate structural aspects of optically active chiral molecules, and to confirm that the peptide bonded to the particles and produced chiral particles. Likewise, the opposite signals obtained at the CD indicate that the electronic structure of the catalyst has chirality on it. The UV-Visible spectra of the nanoparticles are under the CD to compare that the CD has a signal at the same region of the UV-Vis, meaning that the signal acquired is actually from the nanoparticles. The spectra on the bottom is the peptide by itself, which has a signal from 200-270 nm, a different region from the nanoparticles.

The peptide CHA was successfully used as a template to produce chiral cobalt oxide nanoparticles. UV-Visible spectroscopy was used to see the spectral absorbance of the bands corresponding to cobalt oxide, FEG images were acquired to confirm the formation of the nanoparticles, NTA showed the average size, and circular dichroism (CD) spectroscopy was used to investigate structural aspects of optically active chiral molecules, and to confirm that the peptide bonded to the particles and produced chiral particles. X-ray diffraction analysis (XRD) was used to determine the crystallographic structure of the material. These results led to significant results, and further research implies more characterization, to later determine an application for the nanoparticles synthesized with the peptide.